KeAi CHINESE ROOTS GLOBAL IMPACT

Available online at www.keaipublishing.com/en/journals/journal-of-magnesium-and-alloys/

ScienceDirect

Journal of Magnesium and Alloys xxx (xxxx) xxx

www.elsevier.com/locate/jma

Full Length Article

Fabrication and characterization of magnesium-based nanocomposites reinforced with Baghdadite and carbon nanotubes for orthopaedical applications

Mojtaba Ansari[a,*], Shiva Mahdavikia[a], Hossein Eslami[a], Mozhdeh Saghalaini[b], Hamid Taghipour[c], Fatemeh Zare[d], Shahin Shirani[b], Mohammad Hossein Alizadeh Roknabadi[e]

[a] *Department of Biomedical Engineering, Meybod University, Meybod, Iran*
[b] *Department of Biomedical Engineering, Amirkabir University of Technology, Tehran, Iran*
[c] *Center for Education and Research on Macromolecules (CERM), CESAM Research Unit, Department of Chemistry, University of Liège, Liège, Belgium*
[d] *Department of Electrical and Computer Engineering, Texas A&M University, College Station, TX, USA*
[e] *Department of Aerospace Engineering, Amirkabir University of Technology, Tehran, Iran*

Received 7 July 2024; received in revised form 26 November 2024; accepted 1 December 2024
Available online xxx

Abstract

This study explores the potential of Mg/Carbon Nanotubes/Baghdadite composites as biomaterials for bone regeneration and repair while addressing the obstacles to their clinical application. BAG powder was synthesized using the sol-gel method to ensure a fine distribution within the Mg/CNTs matrix. Mg/1.5 wt.% CNT composites were reinforced with BAG at weight fractions of 0.5, 1.0, and 1.5 wt.% using spark plasma sintering at 450 °C and 50 MPa after homogenization via ball milling. The cellular bioactivity of these nanocomposites was evaluated using human osteoblast-like cells and adipose-derived mesenchymal stromal cells. The proliferation and attachment of MG-63 cells were assessed and visualized using the methylthiazol tetrazolium (MTT) assay and SEM, while AD-MSC differentiation was measured using alkaline phosphatase activity assays. Histograms were also generated to visualize the diameter distributions of particles in SEM images using image processing techniques. The Mg/CNTs/0.5 wt.% BAG composite demonstrated optimal mechanical properties, with compressive strength, yield strength, and fracture strain of 259.75 MPa, 180.25 MPa, and 31.65 %, respectively. Machine learning models, including CNN, LSTM, and GRU, were employed to predict stress-strain relationships across varying BAG amounts, aiming to accurately model these curves without requiring extensive physical experiments. As shown by contact angle measurements, enhanced hydrophilicity promoted better cell adhesion and proliferation. Furthermore, corrosion resistance improved with a higher BAG content. This study concludes that Mg/CNTs composites reinforced with BAG concentrations below 1.0 wt.% offer promising biodegradable implant materials for orthopedic applications, featuring adequate load-bearing capacity and improved corrosion resistance.

Keywords: Biodegradable material; Magnesium-based composite; Carbon nanotube; Baghdadite; Spark plasma sintering.

1. Introduction

Bone is a vital tissue in the body, serving various functions such as protecting organs and storing minerals. Bone fractures have long been a challenge for doctors and patients. Therefore, it is imperative to design orthopedic implants that have desirable physiological and physical characteristics capable of serving as stabilizing devices and bone replacements. Ideal bone implants should gradually be replaced with growing bone after the bone regeneration process has finished. They can also degrade uniformly in the human body.

* Corresponding author.
E-mail address: Ansari@meybod.ac.ir (M. Ansari).

https://doi.org/10.1016/j.jma.2024.12.004

Please cite this article as: M. Ansari, S. Mahdavikia, H. Eslami et al., Fabrication and characterization of magnesium-based nanocomposites reinforced with Baghdadite and carbon nanotubes for orthopaedical applications, Journal of Magnesium and Alloys, https://doi.org/10.1016/j.jma.2024.12.004

Furthermore, they usually possess measurable mechanical characteristics such as suitable strength, elastic modulus, and hardness. For adequate stiffness and fracture resistance without looseness or displacement, the values of these mechanical characteristics should be similar to or slightly exceed those of natural bone. Moreover, implants should stimulate bone repair through osteoinduction and osteogenesis in addition to being non-toxic and non-inflammatory in the human body [1]. Using degradable implants in place of damaged tissue is an effective solution, as it minimizes the risks of a subsequent procedure to remove the implant. Additionally, the increasing incidence of musculoskeletal injuries and defects due to aging, sports activities, trauma, and inflammation has led to a growing demand for bone implants, and researchers and doctors are dedicated to finding the most effective and advanced methods in this field. Various materials, including metal, ceramic, and polymer, are used to make implants. Due to these considerations, magnesium alloys have received much attention as candidates for the next generation of biodegradable orthopedic implants due to their biocompatibility, degradability, and osteopromotive properties. In spite of magnesium alloys' superior performance over conventional metallic biomaterials, using pure magnesium as a bone implant still presents several challenges. One of these difficulties is that pure magnesium does not have enough mechanical strength or ductility, and it degrades quickly in the physiological environment before significant bone repair occurs [2]. Rapid magnesium degradation not only compromises the implant's mechanical integrity but also generates a significant amount of H2 gas [3]. Researchers seek ways to control the rate of magnesium degradation during tissue repair. Proposed solutions include alloying, increasing purity, applying mechanical operations, surface modification, and making composites using magnesium.

As part of the process of making magnesium-based composites, choosing the type and amount of reinforcement and the manufacturing method is very important. Studies have shown that different types of reinforcement, such as ceramic biomaterials, metal oxides, carbon, and their derivatives, have been used to make magnesium-based composites. Optimal mechanical and biological performance of magnesium-based implants can be achieved by selecting the appropriate type, amount, and uniform distribution of reinforcing particles. Baghdadite (BAG), a calcium silicate containing zirconium, has demonstrated excellent bioactivity, formed apatite and stimulated cell proliferation. It degrades at a rate sufficient for generating hard tissue. Researchers have been drawn to these ceramics due to their exceptional biological properties, which promote human osteoblast growth, ossification, and mineralization [4]. Additionally, powder metallurgy methods, especially the Spark Plasma Sintering (SPS) method, have been successful in producing magnesium-based composites due to their density and uniform distribution of reinforcement.

Hydroxyapatite (HA) is one of the most common bioceramics used in body implants. Many studies have focused on the use of HA for the construction of implants. Incorporating HA-reinforced particles in AZ91 alloy significantly increased the strength and flexibility of the composite. Furthermore, applying an HA coating to magnesium alloys can enhance the bioactivity, corrosion resistance (CR), and biocompatibility of the substrates, as HA's composition closely resembles that of natural bone tissue. Feng and Han [5] evaluated the mechanical and biological behavior of ZK60A composite reinforced with calcium phosphate particles. Their findings showed that the inclusion of a reinforcing phase led to an increase in the ultimate tensile strength, yield strength, and elastic coefficient of the alloy. Moreover, the corrosion rate gradually decreased with the increase in the reinforcing phase. The mechanical behavior of the Mg/HA composite made by the powder metallurgy method after immersion in Simulated Body Fluid (SBF) solution was evaluated in laboratory conditions. The study highlighted the promising role of HA in enhancing the mechanical stability of magnesium-based composites during the repair of damaged tissue in the body environment [6]. Jaiswal et al. also conducted a study on the mechanical, corrosion and biological behavior of Mg-3 Zn composite reinforced with HA [7]. In another study, the mechanical and corrosion behavior of magnesium-based composites with HA reinforcement made by the SPS method was investigated [8]. Their results indicated that adding HA improved magnesium-based composites' mechanical and corrosion behavior. Huan et al. [9,10] used different percentages of 45S5 bioactive glass as reinforcement to make composites based on ZK30 alloy. They employed semi-solid casting and powder metallurgy methods to produce the composites. The composite containing 10 wt.% of bioactive glass, made by powder metallurgy, exhibited the lowest hydrogen gas release rate. In a similar study, Datta et al. [11] developed a Mg-BG composite by adding 10 wt.% of bioactive glass to pure magnesium. They observed an increase in corrosion resistance compared to pure magnesium. The mechanical behavior of the Mg/xMgO composite, produced by the sputtered melt deposition method, was investigated, and it was observed that adding 1 vol.% magnesium nano oxide to the Mg/xMgO composite resulted in increased yield strength, ultimate strength, and hardness [12]. Shawai et al. [13] produced a composite based on AZ61 alloy containing Reduced Graphene Oxide (RGO) with MgO reinforcement by Selective Laser Melting (SLM). Carbon Nanotubes (CNTs) have garnered significant interest in magnesium matrix composites due to their unique properties. The distinctive honeycomb lattice structure of CNTs provides a high electron density that effectively enhances Corrosion Resistance (CR) [14]. The study of Casas-Luna and his colleagues [15] who studied the Mg-HA composite, showed that the formation of unwanted Mg2Ca intermetallic phase in Mg grain boundaries can be considered the main reason for the decrease in corrosion resistance in the presence of HA [16]. It has been found that the composite reinforced with MgO exhibited higher mechanical properties compared to the AZ61 alloy, with a hardness of 108 HV and a compressive strength (CS) of 241.2 MPa. A composite based on ZK60 alloy reinforced with CNTs was produced using the SPS process. The effect of the temperature of the SPS process and the number of CNTs on the microstructure and mechanical properties of the resulting composite was evaluated. It was

Please cite this article as: M. Ansari, S. Mahdavikia, H. Eslami et al., Fabrication and characterization of magnesium-based nanocomposites reinforced with Baghdadite and carbon nanotubes for orthopaedical applications, Journal of Magnesium and Alloys, https://doi.org/10.1016/j.jma.2024.12.004

shown that pure magnesium has a compressive strength equal to 172 MPa, and the compressive strength of magnesium reinforced with carbon nanotubes is reported to be equal to 224 MPa. Therefore, it can be seen that adding the optimal amount of Baghdadite has increased the compressive strength [13]. Also, in another study, it was found that the compressive strength of Mg-HA alloy in its maximum state was 207.2 MPa [4]. The amount of hardness in SPS sintered samples depends on various parameters such as relative density (representative of internal porosity), grain size, type and amount of reinforcement, and surface magnesium oxide amount, as well as operational dependent parameters such as SPS process temperature and pressure. Studies showed that samples with higher porosity had lower load-bearing capacity [17]. In addition to the strengthening role of BAG, the relative density has played an important role in determining the compressive strength, and the lower relative density of the Mg-HA alloy and the weak bonds between the HA particles are the main reasons for the low compressive strength was compared to Mg/CNTs/BAG alloy. On the other hand, the increase in the relative density of the resulting composites can be another reason for improving the mechanical behavior of the samples compared to the mentioned study. It can be stated that the higher density was due to the use of the SPS method compared to the cold press method [13]. Furthermore, the role of adding CNT reinforcement on the corrosion behavior of AZ31B alloy was investigated. For this purpose, AZ31B/CNTs composite was made by the SPS method at a temperature of 550 °C and under a pressure of 30 MPa [18]. In the context of the reaction between magnesium and carbon, it should be stated that it has been proven thermodynamically that the formation of metal carbides depends on the Gibbs free energy. Metals such as magnesium, which have a positive free energy, generally do not form magnesium carbides, and/or if they do, they will not be stable at a certain temperature, hence, no reaction between magnesium and CNTs has occurred [13].

Several studies have demonstrated that adding CNT reinforcement to composites can reduce their corrosion susceptibility. Reviews on CNTs reveal that CNTs possess a higher agglomeration tendency than graphene nanoplatelets (GNPs) and fullerenes [19, 20]. The morphological characteristics of metal matrices and carbon nanomaterials, including CNTs, GNPs, and fullerenes, influence their adsorption modes. CNTs, with their high aspect ratios and nanoscale dimensions, present challenges as a reinforcing material in metal matrices [20]. Research has demonstrated that by carefully selecting the optimal percentage of CNTs, it is possible to enhance both the mechanical properties and corrosion resistance of the composite. For example, it has been reported that an optimal amount of CNT reinforcement can significantly improve the mechanical strength and corrosion resistance of the magnesium-based alloy AZ61. Composites with lower amounts of CNT reinforcement have been found to exhibit higher corrosion resistance compared to those with higher amounts of CNTs [21]. In another study, the reinforcing effect of CNTs on the compressive strength of AZ91 and AZ61 alloys was investigated. AZ91-CNTs and AZ61-CNTs composites in this study were produced by cold pressing method. According to their results, the highest compressive strength was obtained for AZ61 alloy containing 0.5 % by weight of CNTs and for AZ91 alloy containing 0.5 % by weight, which were 168.40 MPa and 153.50 MPa, respectively [13]. CNTs show great promise for strengthening magnesium matrices while simultaneously lowering corrosion rates and preventing the production of H2 gas. These investigations provide insight into the improvements in strength and ductility of CNT-reinforced composites as well as their microstructural evolution, which can be examined using several mechanical tests. Utilizing machine learning techniques to predict material properties, such as stress-strain curves, has gained substantial attention due to its ability to handle complex, non-linear data. Traditional models rely heavily on physical laws or empirical relations, but neural networks provide a data-driven approach that can capture intricate patterns directly from experimental data. In the concept of mechanical tests, predicting the stress-strain behavior of these composites accurately is critical for streamlining the material design process [22]. These models can provide rapid, reliable predictions based on the mechanical dataset, significantly reducing the need for extensive experimental testing.

It has been stated that sintering occurs in the common phase of magnesium particles much better compared to magnesium particles and Baghdadite, which is due to the difference between the temperature of the sintering process and the melting point of the powder particles. Such behavior has also been observed in other studies, for example, Nakahata et al. [8] observed for HA-reinforced magnesium composite that with the increase of HA content, the porosity of the sintered sample increased due to the difference between the SPS temperature, and the melting point of powder particles has increased. However, they found that the smaller the magnesium particle size, the lower the porosity. It was reported that fine magnesium particles can fill the space between the particles and increase the relative density. In the field of relative density of composites sintered by the SPS process, various parameters are effective. These parameters can be classified into two groups (1) characteristics of the used powder such as size, and melting point, and (2) operational characteristics of the SPS process such as temperature and process pressure. For example, it was shown that by increasing the temperature to a critical level, due to the reduction of the distance between the powder particles and the increase of their contact surface due to the higher temperature, the density increases. On the other hand, in the field of SPS process pressure, it can be stated that pressure through mechanical effectiveness can improve the way particles are placed next to each other and also lead to the crushing of agglomerate particles, especially in the field of nanometer powders. All of which increase the relative density of matter. Also, applying pressure increases the driving force for sintering, which can decrease the temperature required for the SPS process [19,20].

CNTs, known for their high strength and electrical conductivity, exhibit variable degradation behavior depending on their form and the matrix they are incorporated into. Studies

Please cite this article as: M. Ansari, S. Mahdavikia, H. Eslami et al., Fabrication and characterization of magnesium-based nanocomposites reinforced with Baghdadite and carbon nanotubes for orthopaedical applications, Journal of Magnesium and Alloys, https://doi.org/10.1016/j.jma.2024.12.004

have shown that CNTs can degrade at a controlled rate in biological environments, which can be beneficial for maintaining long-term mechanical support for implants. Combining these materials (CNTs and BAG) with magnesium in composite structures aims to optimize both the mechanical performance and the degradation profile, ensuring the implants support bone healing effectively while gradually integrating into the body. There is still a lack of extensive research on how CNTs and the defects in their sp^2-hybridized carbon structure, formed at various stages of the composite manufacturing process, influence their capability to reinforce Mg matrices. Additionally, in vitro cytotoxicity and corrosion behavior of Mg-based composites enhanced with CNTs remain underexplored. Mechanical properties as well as biodegradability tests on pure magnesium matrices containing CNTs have also not been thoroughly studied. Recent studies indicate that the unique honeycomb lattice of CNTs gives them a high electron density, making them highly suitable for applications requiring enhanced corrosion resistance [14]. Nevertheless, CNTs tend to agglomerate more than other nanomaterials such as graphene nanoplatelets and fullerenes due to their high aspect ratios and nanoscale dimensions [21]. Similarly, Baghdadite, a calcium silicate containing zirconium, has demonstrated good bioactivity by forming apatite and promoting cell proliferation, making it an appealing choice for bone repair [4].

This study presents a cytotoxic, corrosion, and mechanical evaluation of Mg matrices enhanced with CNTs and Baghdadite, fabricated using Spark Plasma Sintering (SPS). The research investigates the effects of varying weight fractions of Baghdadite (0.5–1.5 wt.%) within Mg/CNTs matrices and compares the results. To minimize the agglomeration of CNTs within the Mg matrices, a low concentration of CNTs (1.5 wt.% relative to Mg) was used. This approach reduces the risk of micro-galvanic corrosion, which can occur when CNTs act as cathodic sites in corrosive environments. Although magnesium's high corrosion rate and limited mechanical stability have constrained its applications, strategies such as enhancing magnesium purity, applying surface coatings, alloying, and creating composites have been proposed to overcome these challenges [3]. Recent advancements in magnesium-based composites for bone implants have gained attention recently, and the type and amount of reinforcement, as well as the manufacturing method, play a crucial role in determining their performance. Various reinforcements, including bioceramics, metal oxides, and carbon derivatives, have been utilized for these composites. The SPS method has proven to be an ideal and controllable technique for fabricating composites from a mixture of primary powders. This research aims to fabricate and characterize a magnesium-based nanocomposite reinforced with Baghdadite and CNTs for implantable and orthopedic applications using SPS. Additionally, implants' efficiency is evaluated using several approaches including mechanical tests like the implants' stress behavior due to the increase in strain, and then estimated for other composition measures with Baghdadite using machine learning approaches.

2. Materials and methods

2.1. Starting materials

Powders of pure magnesium (45-micron particle size, 99.9 % purity) (Merc, Germany) and CNTs (20–30 μm outer diameter, 10–30 μm length, 95 % purity) (Titra Chem, Canada) were used in this study as elemental powders. Other materials that were used in this study are listed in Table 1 along with their specified applications and chemical composition.

2.2. Synthesis of baghdadite powder

Baghdadite powder was synthesized using the sol-gel method. Firstly, tetraethyl orthosilicate (TEOS), ethanol, and HNO_3 (2 M) were mixed in a 1:8:0.16 molar ratio and stirred for 30 min using a magnetic stirrer. Zr, Ca, and Si raw materials with a 1:3:2 molar ratio were then added to the solution and stirred for 5 h The resulting solution was heated at 60 °C for 1 day and then at 100 °C for 2 days. The dried gel was then annealed at 1150 °C for 3 h [23].

2.3. Synthesis of Mg/CNTs/BAG composites

To investigate the role of Baghdadite as reinforcement in Mg/CNTs alloys, four different samples were prepared with varying amounts of Baghdadite to form the Mg/CNTs/BAG composite. The synthesis process began by measuring the powders according to specific weight ratios. Baghdadite and CNTs were dispersed into Mg powder using solution mixing and planetary ball milling (BM) techniques. Initially, CNTs were added to the Mg powder at a weight fraction of 1.5 wt.%, followed by the addition of Baghdadite at weight fractions of 0.5, 1, and 1.5 wt.%. These powders were then ball-milled using a custom-made planetary ball mill with chromium-rich stainless-steel components. Before mixing, each powder was separately dispersed in ethanol and ultrasonicated for 30 min to stabilize the colloidal suspensions. The CNTs dispersed in the Mg solution were then combined with the Baghdadite solution, and the ultrasonication process was continued for an additional 10 min to ensure uniform nanoparticle dispersion within the base solution. The ball milling of the Mg/CNTs/BAG powders was conducted at 900 rpm for 10 h in an inert atmosphere to prevent contamination. Five stainless steel balls, each with a 20 mm diameter, were used during the milling process. After ball milling, the pre-dried powder mixtures were heated to 140 °C for 4 h in a vacuum oven to remove ethanol and prevent void formation before sintering. The dried powders were then compacted using a uniaxial hydraulic press under a pressure of 50 MPa for 20 min. Subsequently, the samples underwent spark plasma sintering at 450 °C under vacuum conditions, using a DC pulse (0–20 V, 104 A, 200 Hz) at a heating rate of 50 °C/min for 3 h. The density of the sintered samples was determined using Archimedes' principle in accordance with ASTM B962–15 standards [24].

Please cite this article as: M. Ansari, S. Mahdavikia, H. Eslami et al., Fabrication and characterization of magnesium-based nanocomposites reinforced with Baghdadite and carbon nanotubes for orthopaedical applications, Journal of Magnesium and Alloys, https://doi.org/10.1016/j.jma.2024.12.004

Table 1
Materials needed for making Mg/CNTs/BAG composite and materials needed for making body simulator solution for corrosion test.

Material	Chemical combination	Producer	Application
Tetraethyl orthosilicate, 98 % purity	$C_8H_{2n}O_4Si$	MERC	Synthesis of Baghdadite
Zirconium oxynitrate, 98 % purity	$ZrO(NO_3)_2$	MERC	Synthesis of Baghdadite
Calcium nitrate tetrahydrate	$Ca(NO_3)_2{\cdot}4H_2O$	MERC	Synthesis of Baghdadite
Ethanol, 99.99 % purity	C_2H_5OH	Kimia alcohol zanjan	Powder mixing solution
Sodium chloride	NaCl	MERC	Making a body simulating solution
Potassium chloride	KCL	MERC	Making a body simulating solution
Magnesium chloride six-hydrate	$MgCl_2{\cdot}6H_2O$	MERC	Making a body simulating solution
Dipotassium hydrogen phosphate trihydrate	$K_2H_PO_4{\cdot}3H_2O$	MERC	Making a body simulating solution
Calcium chloride	$CaCl_2$	MERC	Making a body simulating solution
Sodium phosphate	Na_2SO_4	MERC	Making a body simulating solution
Hydrochloric acid	HCl	MERC	Making a body simulating solution
Sodium hydrogen carbonate	$NaHCO_3$	MERC	Making a body simulating solution

2.4. Characterization of powder mixtures and sintered composites

A morphological analysis of the synthesized Baghdadite powders was analyzed using conventional scanning electron microscopy (Philips XL30) in secondary electron mode. Before imaging, the samples were gold sputtered under vacuum with an argon flux, utilizing an electric current of 30 mA and a voltage of 30 kV. The distribution of particle sizes was determined by using the ImageJ and MATLAB softwares, following ISO 13,322–1:2014 guidelines [25]. The phase composition of the Baghdadite powder, Mg/CNTs/BAG ground samples, and sintered compacts was identified using X-ray diffraction (XRD) analysis. An XRD machine (AW-XDM300, Asenware, China) with Cu-Ka α radiation ($\lambda = 1.5418$ Å) was operated with a scanning rate of 0.03°/s over a 2θ angular range of 10–90° The diffractometer operated at 40 kV and 30 mA, and the phases were analyzed using XpertHighscore software. The microstructures of the Mg/CNTs alloys and Mg/CNTs/BAG composites were examined using a field emission scanning electron microscope (FESEM) equipped with an EDAX Energy Dispersive X-ray Spectroscopy (EDS) system for elemental analysis. To assess the surface wettability and hydrophilicity of the composites, contact angle (CA) measurements were conducted. These measurements were performed at 20 °C using a GBX Digidrop instrument (DGD Fast 60 Contact Angle Meter) provided by Apex Technologies. Static contact angles were calculated as the average of at least four measurements on different positions of each specimen. A droplet (~1 μL) was deposited on the surface, and temporal images were captured with a digital camera 4 s after deposition. The contact angle values were then calculated using WinDrop software based on the obtained images.

2.5. Mechanical property testing

The properties of sintered Mg/CNTs alloys and Mg/CNTs/BAG composites with varying Baghdadite percentages (0.5–1.5 wt.%) have been evaluated following ASTM E9–89a standards. Compression measurements were conducted on a uniaxial 5 kN testing machine from Instron at a displacement rate of 0.5 mm/min. For these tests, three cubic samples from each batch, measuring 10 × 10 × 10 mm^3, were prepared. Additionally, the Vickers microhardness (Hv) of the samples was measured using a Zwick/Roell Zhu 2.5 hardness tester (Zwick GmbH & Co. KG, Germany). The test was performed under a load of 0.05 kg for ten seconds, and each specimen was tested three times to ensure accuracy.

2.6. Deep learning models for stress-strain curve prediction

Three artificial neural models—Convolutional Neural Networks (CNN), Long Short-Term Memory (LSTM) networks, and Gated Recurrent Units (GRUs)—for the prediction of stress-strain curves in composite materials. Each model offers unique advantages in processing the sequential data obtained from the material's mechanical properties. CNNs are known for their capability to efficiently extract local features from structured data, such as images or sequential signals [26]. The LSTM network is a variant of recurrent neural networks designed to handle long-term dependencies in sequential data [27]. LSTMs address the vanishing gradient problem, allowing them to capture patterns over long time steps. GRUs are another form of recurrent neural networks, but with a simpler architecture compared to LSTMs, making them computationally more efficient while still maintaining the ability to capture long-term dependencies [28].

2.7. Degradation behavior of fabricated Mg/CNTs/BAG composites

A deterioration process in manufactured Mg/CNTs/BAG materials has been evaluated using electrochemical analysis. The tests were conducted on disc-shaped samples measuring a diameter of 10 mm and a thickness of 3 mm. Potentiodynamic (PD) polarization curves were recorded over a scanning range of ±250 mV relative to the Open Circuit Potential (OCP) at a scanning rate of 1 mV/s, utilizing an AMETEK PARSTAT 2273 electrochemical workstation. The testing setup employed a three-electrode cell configuration, comprising an Ag/AgCl electrode, a platinum counter electrode (1.5 cm^2), and cold mounted samples on the working electrode. The mounted samples were immersed in a corrosion solution for 30 h at 37 °C in order to stabilize their open circuit potential. The

Please cite this article as: M. Ansari, S. Mahdavikia, H. Eslami et al., Fabrication and characterization of magnesium-based nanocomposites reinforced with Baghdadite and carbon nanotubes for orthopaedical applications, Journal of Magnesium and Alloys, https://doi.org/10.1016/j.jma.2024.12.004

corrosion current density (i_{corr}, μA) and Dissolution Corrosion Rates (DCR) were determined through Tafel extrapolation using Powersuite software. To further assess the degradation behavior, the mounted samples were soaked in a SBF solution with a pH of approximately 7.4 at a temperature of 37 ± 1 °C. Three samples of the composites have been tested by electrochemical evaluation. OCP also performed electrochemical impedance spectroscopy (EIS) within the frequency range of 100 kHz to 100 MHz. The resulting data were analyzed and visualized as Nyquist and Bode plots using EClab and ZView2.0 software. An equivalent electrical circuit was derived by fitting the obtained data to model the system's behavior.

2.8. In-vitro biocompatibility assessment of Mg/CNTs/BAG composites

Cell toxicity of Mg/CNTs/BAG composites was evaluated by the use of osteoblastic MG-63 cells (NCBI, Pasteur Institute, Iran) based on procedures described in ISO 10,993–1:2009 [29]. Before testing, the composite specimens were cleaned with acetone, ethanol, as well as water for 15 min each. Extracts were prepared by immersing the composites into Modified Dulbecco's Eagle Medium (DMEM-F12, Gibco, Paisley, UK) containing Fetal Bovine Serum (10 %) (Biowest, Nuaille, France) at a surface area-to-medium ratio of 0.8 cm²/mL. These were incubated in a humidified environment (95 % H_2O, 5 % CO_2 at 37 °C) for 1, 2, and 3 days. The supernatants were then collected, filtered sterilized using a 0.22 μm filter (Falcon, BD Biosciences, USA), and stored for further analysis. Control extracts were prepared similarly but without the addition of the composite materials. MG-63 cells were seeded in 96-well plates with 20,000 cells per well, using 100 μL of supplemented DMEM. After incubating for 24 h to allow cell attachment, the medium was replaced with 100 μL of the prepared extracts, while control wells received fresh supplemented DMEM. The cells were cultured for three days, reaching a confluency of 80–90 %, and cytotoxicity was assessed using the MTT assay [30–32]. Cells were incubated with the extracts for 24, 48, and 72 h. Following incubation, a fresh medium containing 0.5 mg/mL MTT solution was added, and cells were allowed to incubate for four hours at 37 °C in a humidified environment. Crystals of formazan formed within cells were dissolved in Dimethyl Sulfoxide (DMSO), and the resulting solution was transferred to a new plate for optical density (OD) measurement. Using a spectrophotometer (BIOTEK EL808), absorbance was read at 570 nm. The viability of the cells exposed to the composite extracts was compared to the control group, and the results indicated the percentage of viable cells relative to the control. ALP activity of adipose-derived mesenchymal stem cells (AD-MSCs) cultured on Mg/CNTs and Mg/CNTs/BAG composites was evaluated over 3, 7, and 14 days. Circular specimens (1.5 cm in diameter) were inserted into a 48-well plate and pre-incubated in a normal medium (DMEM with 10 % FBS) overnight to promote attachment of the cells. Trypsinized AD-MSCs were seeded on composites at 20,000 cells/well, with control cells cultured on Tissue Culture Polystyrene (TCP). After 30 min, the wells were filled with normal medium to a final volume of 500 μL. On the following day, the medium was replaced with osteogenic medium, which was refreshed weekly over 3, 7, 14, and 21 days. At the end of the incubation periods, the cells were washed with PBS, fixed in 10 % formalin, and stained with an ABCIP-NBT solution (5–bromo-4–chloro-3-indolyl phosphate/nitro blue tetrazolium). ALP activity was visualized as the development of blue staining and quantified using an ALP assay kit (Pars Azmun, Tehran, Iran). A mixture of KOH and DMSO was used to dissolve the stained samples, and their absorbance was measured at 405 nm. The total protein content of the samples was used to normalize ALP activity. All tests were conducted three times to ensure accuracy. For identifying significant differences ($p < 0.05$) in cell proliferation and ALP activity, two-way ANOVA was used with a Bonferroni post hoc test. GraphPad Prism version 6 was used to visualize the results.

2.9. Statistical analysis

The statistical analysis was conducted using GraphPad Prism 6 software (GraphPad Software, Inc., La Jolla, CA). The corresponding statistical analyses are described in the following paragraph. Each group of samples underwent three separate trials for compression testing, corrosion testing, and in vitro cytotoxicity evaluation to ensure consistency and reliability of the results.

3. Results and discussion

3.1. Morphology and phase composition

The morphology of the synthesized Baghdadite is shown in Fig. 1, which contains the SEM images and corresponding particle size distributions of the bulk powder. From Fig. 1(a), it is evident that the powder shows an irregular morphology with a high degree of agglomeration while entangled CNT particles typically possess an agglomerated morphology [33]. It is also obvious from the high magnification morphology that the synthesized Baghdadite possess a porous geometry with interconnectivity and fine grain size distributions. Image analysis revealed that the particle size limit of agglomerated BAG powder is <30 μm, affirming the successful synthesis of porous Baghdadite using the sol-gel method (Fig. 1(b)). Previous research revealed that the porous Baghdadite with fine grain size distributions are essential for bone regeneration [4,34].

The XRD analysis finding of the BAG nanoparticles is shown in Fig. 2(a). The XRD pattern of the synthesized powder matches the standard XRD pattern of Baghdadite (Standard Cards No 00–047–1854). As can be seen in Fig. 2(a), all the peaks correspond to the characteristic peaks of Baghdadite (00–047–1854), however, a negligible amount of minor phases (e.g., gittinsite-01–084–2099) has been detected as well [35]. A recent study on SPS of B4C–TiB2 composites has revealed

Please cite this article as: M. Ansari, S. Mahdavikia, H. Eslami et al., Fabrication and characterization of magnesium-based nanocomposites reinforced with Baghdadite and carbon nanotubes for orthopaedical applications, Journal of Magnesium and Alloys, https://doi.org/10.1016/j.jma.2024.12.004

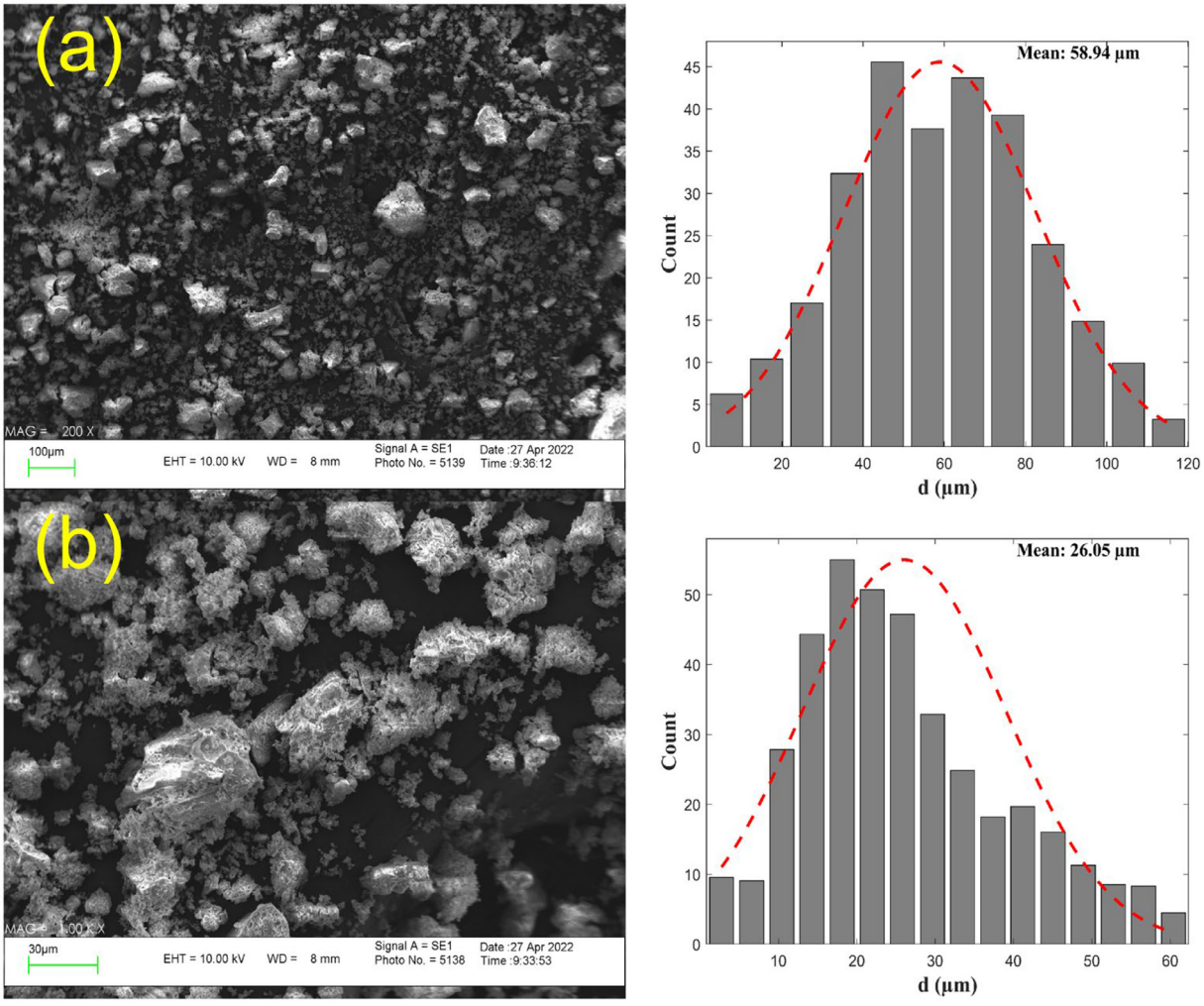

Fig. 1. SEM micrographs of synthesized Baghdadite along with their particle size distributions. Magnification: (a) 200 ×, (b) 1000 × .

that the milling treatment is crucial to achieving a homogenous mixture of powders before the sintering process [36]. In principle, strengthening Mg matrices is mostly dependent on the phase changes, bonding between CNTs and BAGs, and their chemical stability. Fig. 2(b) displays the XRD patterns of the powder mixtures after the grinding process for 10 h. The major peaks in XRD spectra of milled powders are attributed to Mg, despite the presence of some crystalline Mg commercially available. The HCP Mg crystal used in this study exhibits three peaks of 32°, 34°, and 37°, corresponding to the (1 0 0), (0 0 2), and (1 0 1) planes. Card number 089–01–4244 (Standard cards). The results confirm that the addition of enhancers did not significantly impact magnesium's intensity and diffraction angle. Due to a low content in CNTs and BAGs, XRD patterns generally are unable to identify CNTs and BAGs peaks. Additionally, there are no signs of the new phase formation in the composite with CNTs and BAGs, suggesting chemical stability for nanoparticles. It is worth mentioning that while some studies have observed peaks in magnesium oxide (MgO) in XRD pattern as a result of the interaction between magnesium and oxygen during the BM [37,38], no MgO peak was observed in this study (e.g., 42.98° and 62.36° correspond to (0 0 2), and (2 0 2) planes respectively), suggesting that the grinding process was conducted without contaminating the powder mixture.

3.2. Microstructure and density of Mg/CNTs/BAG composites

Correlating the reinforcing efficiencies of Mg/CNTs/BAG in response to the processing conditions requires robust characterization of microstructural changes in hybridized carbonaceous reinforcements (such as CNTs/BAG) and interactions with the surrounding metal matrices. Fig. 3 shows the SEM and corresponding EDX elemental maps of the Mg/CNTS/BAG composites containing 1.5 wt.% CNTs and 0.5–1.5 wt.% BAG. The addition of BAGs caused microstructural changes in the Mg metal matrix. Fig. 3(a–d) shows the SEM images and corresponding EDX elemental maps showing the dispersion BAGs in Mg/CNTs. From the figures, Mg/CNTs/x-BAG ($x = 0$, 0.5, 1, and 1.5 wt%) powder mixtures exhibited an irregular morphology with the same particle size (∼ 151.56–102.16 Mm). It is evident that uniform distribution of CNTs was achieved in these batches of composites, as shown by the C elemental maps. The dark

Please cite this article as: M. Ansari, S. Mahdavikia, H. Eslami et al., Fabrication and characterization of magnesium-based nanocomposites reinforced with Baghdadite and carbon nanotubes for orthopaedical applications, Journal of Magnesium and Alloys, https://doi.org/10.1016/j.jma.2024.12.004

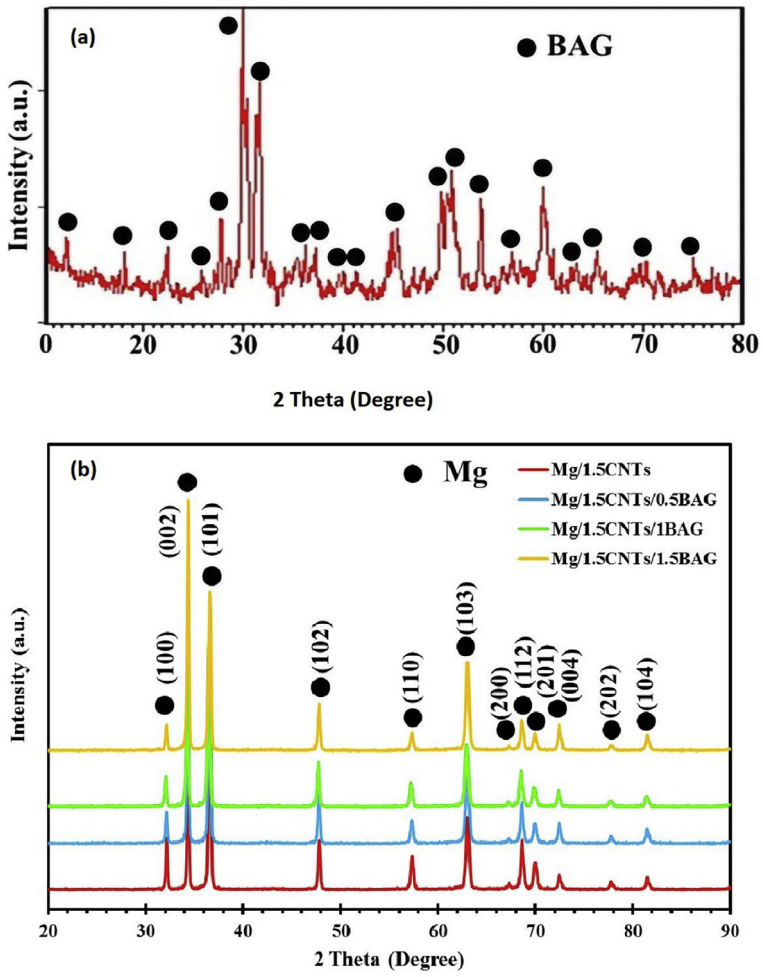

Fig. 2. XRD pattern of (a) BAG nanoparticles matching the Baghdadite standard (00–047–1854) with minor gittinsite phases. (b) the powder mixture used to make Mg/CNTs/BAG composite after 10 h of mechanical grinding.

regions in the O elemental maps correspond to oxidation in the fabricated composites during the grinding and subsequent sintering processes which merely decreased with an increase in BAG content in the Mg/CNTs matrices. This might be explained by the relatively high surface areas of CNTs, which give them a strong affinity towards oxygen and result in the formation of magnesium oxide on the surface of the powder particles [39]. Previous studies reported that the presence of magnesium oxide affects the bond between the metal matrices and the reinforcements, which can adversely affect the resultant strength of the composites [40,16]. As will be explained later, this is supplemented by XRD patterns that were taken from the fabricated composites. From the Zr, Ca, and Si elemental analysis, it is evident that the BAG reinforcing powders were well distributed in the magnesium matrices, facilitating the creation of a composite with a homogeneous structure and uniform dispersion of the reinforcements. The average relative density of the sintered Mg/CNTs compact was measured as 99.4 %. Compared to the Mg/CNTs compact, the addition of BAGs resulted in a decrease in densification of the Mg/CNTs/BAG composites fabricated under similar conditions. For the sintered Mg/CNTs/BAG composites reinforced with BAGs, average relative densities were measured as 99.1 %, 98.8 %, and 98.7 % with the addition of 0.5, 1.0, and 1.5 wt.% BAGs, respectively. The decrease in the relative density of the composites with an increase in BAG content (Table S1 from supporting information) may be attributable to their stacking due to the different nature of Baghdadite as a ceramic and magnesium as a metal, which increases the strength of their common phase bonding during the high-temperature plasma sintering process. In particular, this causes an increase in the porosity of the hybrid content at the contact point of ceramic/metal in the composite structures and further reduction of their relative density. To further verify whether BAG content plays a role in the addition of porosity and further reduction of the density of Mg/CNTs/BAG composites, we studied the SEM images of the sintered composites, as shown in Fig. S7 (see supporting information). As is obvious from this figure, with the increasing amount of the BAG content from 0 to 1.5 wt%, the mean porosity size of the composites has magnified.

Fig. 4 shows the XRD patterns of the sintered Mg/CNTs alloy and Mg/CNTs/BAG composites containing 0.5–1.5 wt.% BAGs. The XRD patterns revealed intense peaks associated

Please cite this article as: M. Ansari, S. Mahdavikia, H. Eslami et al., Fabrication and characterization of magnesium-based nanocomposites reinforced with Baghdadite and carbon nanotubes for orthopaedical applications, Journal of Magnesium and Alloys, https://doi.org/10.1016/j.jma.2024.12.004

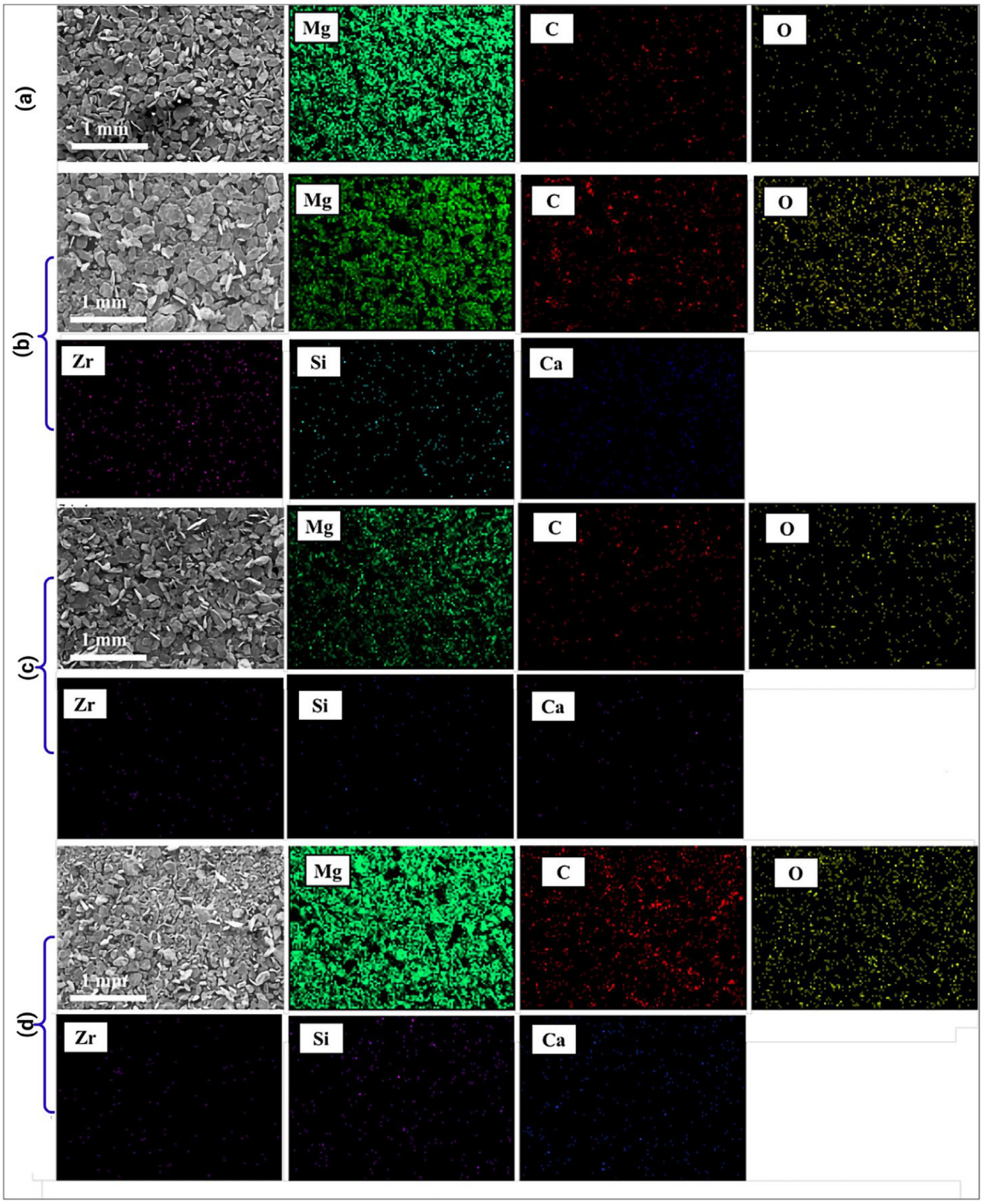

Fig. 3. SEM images, and corresponding EDX elemental maps of fabricated Mg/CNTs/BAG composites: (a–d) SEM images and corresponding elemental maps of Mg/CNTs/BAG composites: (a) Mg-1.5 wt.% CNTs; (b) Mg-1.5 wt.% CNTs-0.5 wt.% BAG; (c) Mg-1.5 wt.% CNTs-1.0 wt.% BAG.

with Mg along with less intense peaks at 2θ of ~26° and ~43° associated with CNTs and MgO respectively. The intensity of the MgO phase didn't show considerable change with increasing content of BAGs dispersed in the Mg/CNTs matrices. This may be attributable to defect accumulation in the CNTs which have a high affinity to absorbing available oxygen atoms in the atmosphere during the processing of Mg/CNTs/BAG composites.

SEM and EDX maps also confirmed the presence of oxygen in the grain boundaries as shown in Fig. 3(a–d). This is in agreement with the previous study on the defect formation of carbon nanomaterials such as GNPs during composite processing in which the defects (in the form of broken edges and vacancies) in their network become active sites for the attachment of functional groups such as oxygen [37,41]. Previous studies have shown, on the one hand, that the sintering

Please cite this article as: M. Ansari, S. Mahdavikia, H. Eslami et al., Fabrication and characterization of magnesium-based nanocomposites reinforced with Baghdadite and carbon nanotubes for orthopaedical applications, Journal of Magnesium and Alloys, https://doi.org/10.1016/j.jma.2024.12.004

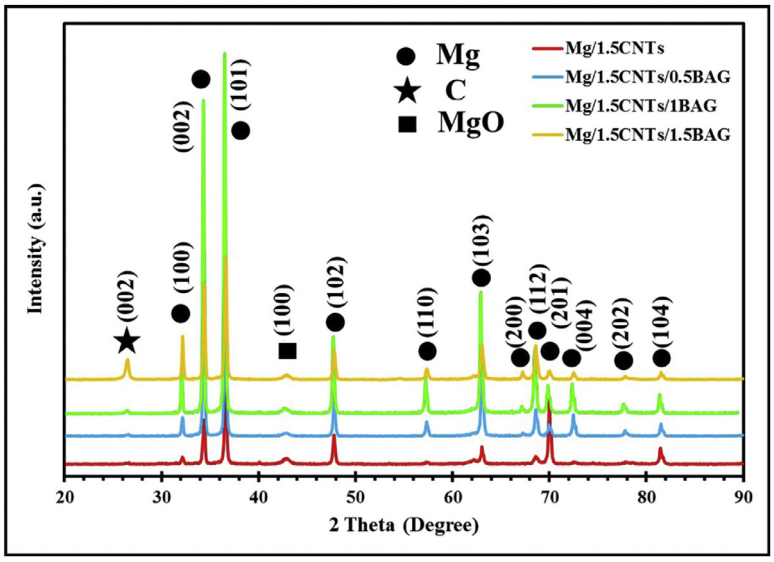

Fig. 4. XRD pattern of Mg/CNTs/BAG composites synthesized under a pressure of 50 MPa and at a temperature of 450 °C.

time has a significant role in the formation of MgO compared to the processing temperature [40]. On the other hand, it has been reported that adequate temperature and pressure during the SPS process can lead to the evaporation and bond breakage of the oxide layers from the grain boundaries and the formation of new short-range interactions between particles which can cause more compaction of the produced composite [16].

3.3. Mechanical properties

Microhardness and compressive strength analyses are presented in Fig. 5(a-f) and Table S2 (supporting information). Vickers hardness measurements for the Mg/CNTs/BAG composites showed a significant increase, rising from 45.00 ± 5.00 HV to 83.00 ± 5.00 HV as the BAG content increased from 0 to 1.5 wt.%. This improvement is due to the presence of the harder BAG phase on the particle surface, which contributes to refining the composite's grain microstructure. Unlike the relative density trend, which is influenced by internal porosity, the strong phase of BAG resists plastic deformation caused by indentation [32,42–44]. Young's modulus (E), ultimate compressive strength (σ_{ucs}), and failure strain values of the Mg/CNTs/BAG composites also improved with increasing BAG weight fractions. For the Mg/1.5 CNTs alloy, the Young's modulus, ultimate compressive strength, and failure strain were measured as 1.91 GPa, 169.75 MPa, and 30.01 %, respectively. When BAG was incorporated at 0.5, 1, and 1.5 wt.%, Young's modulus of the Mg/CNTs/BAG composites was 2.56 GPa, 2.53 GPa, and 2.72 GPa, respectively. Although the modulus values increased for the specimens, they did not exhibit a consistent trend when analyzed under static scanning conditions.

This analysis highlights the structural integrity of Mg composites, indicating their ability to achieve stiffer morphologies. This is demonstrated by their improved capacity to withstand deformation, which reflects the strong interlocking (tangling) between the matrix and reinforcements. The microstructural changes observed in the composites, as revealed by SEM and XRD analysis, show refined grain boundaries and increased crystallinity, contributing to a higher Young's modulus of elasticity. These mechanical properties align closely with those of human bones [1,45]. The ultimate compressive strength (σUCS) for Mg/CNTs/BAG composites with 0.5, 1, and 1.5 wt percent BAG was measured at 180.25 MPa, 105.65 MPa, and 83.70 MPa, respectively. Similarly, failure strains (ε) for mixtures with 0.5, 1, and 1.5 wt percent BAG were recorded at 31.65 %, 20.35 %, and 17.25 %, respectively. The compressive strength and failure strain peaked at 180.25 MPa and 31.65 % with 0.5 wt% BAG, surpassing the values for the Mg/1.5CNTs alloy (169.75 MPa and 30.01 %). This improvement is attributed to the superior mechanical properties of BAG's crystalline structure, such as its high fracture toughness and hardness, which contribute positively to the composite's performance at lower BAG fractions [4,46]. However, as the BAG content exceeded 1 wt%, both compressive strength and failure strain declined. This reduction is attributed to the agglomeration of BAG nanoparticles, which negatively affects the uniformity and coherence of the composite structure [47,48]. Despite this, the integration of BAG up to 0.5 wt% effectively refines the grain size and facilitates load transfer from the α-Mg matrix to the stiff CNT nanoparticles coated with BAG additives, enhancing the mechanical characteristics of the Mg/CNTs alloy [30]. At the interface between the Mg matrix and CNTs, dislocations are generated due to the mismatch in thermal expansion coefficients (26×10^{-6} K^{-1} for Mg and 2×10^{-5} K^{-1} for CNTs). These dislocations strengthen the composite by resisting movement across the interface, following the Orowan strengthening mechanism [32,49–51]. Conversely, excessive BAG content (1.5 wt percent) disrupts this

Please cite this article as: M. Ansari, S. Mahdavikia, H. Eslami et al., Fabrication and characterization of magnesium-based nanocomposites reinforced with Baghdadite and carbon nanotubes for orthopaedical applications, Journal of Magnesium and Alloys, https://doi.org/10.1016/j.jma.2024.12.004

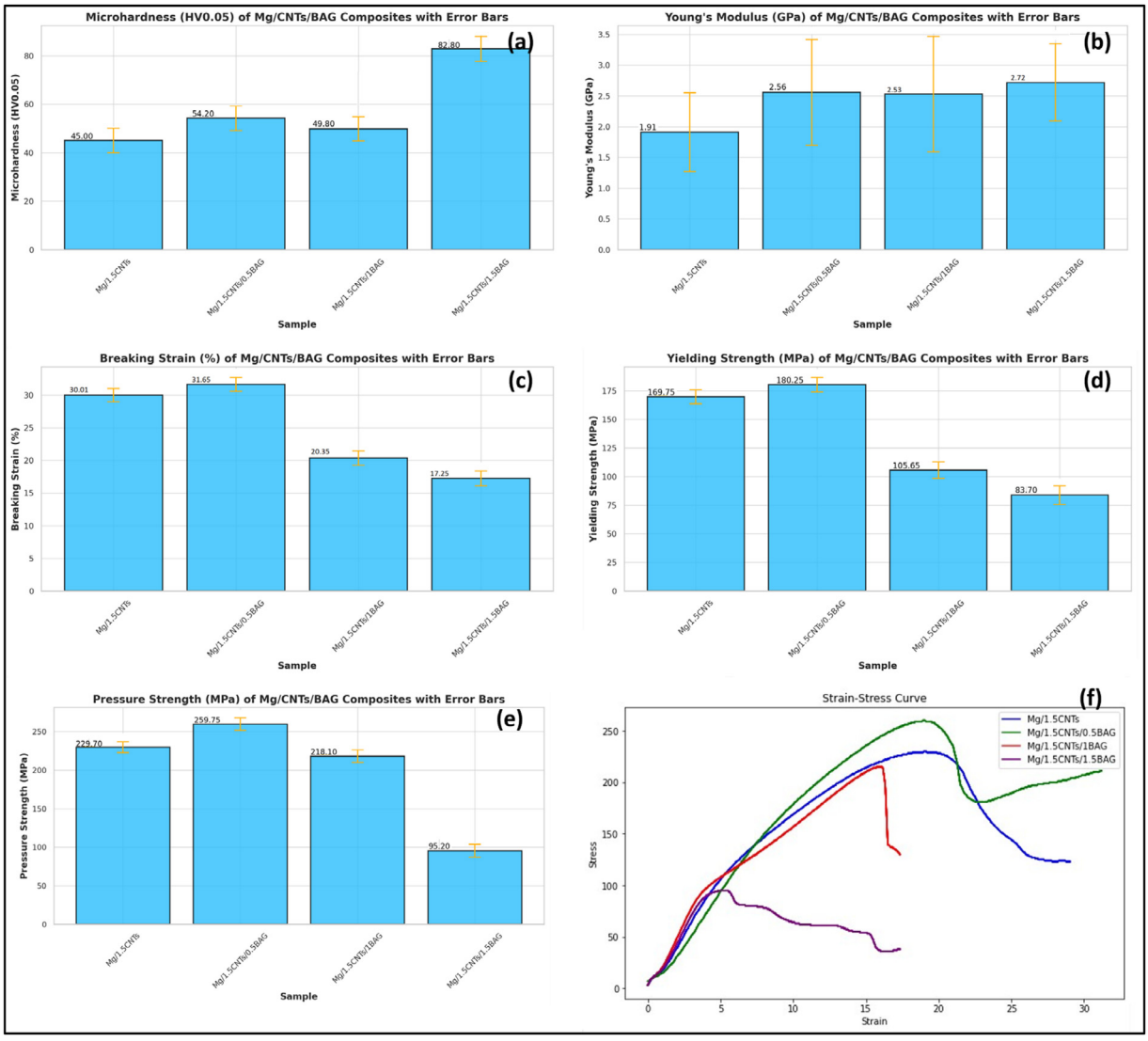

Fig. 5. (a) Average Microhardness (Hv); (b) Young Modulus (GPa); (c) Breaking Strain (%); (d) Yielding Strength (Mpa); (e) Pressure Strength (Mpa); (f) Compressive stress-strain curves (Eng Stress (MPa) vs Eng Strain of Mg/CNTs/xBAG (x = 0, 0.5, 1 and 1.5 wt%) with error bars.

mechanism by preventing the formation of strong and coherent joints between BAG particles and the Mg/CNT matrix, resulting in a decrease in mechanical properties. According to the results, Mg/CNTs/0.5 BAG (259.75 MPa) is higher compared to Mg/CNTs/1.0 BAG (218 ± 8 MPa), Mg/CNTs/1.5 BAG (95 ± 8 MPa), Mg/CNTs (229.7 ± 7 MPa), AZ91–0.5CNTs (153.5 MPa) [52], AZ61–0.5CNTs (168.4 MPa) [52], Mg-0.5Zr/0.1GNPs (219 ± 3 MPa) [53], Mg-3Zn-1Mn (244.5 ± 9 MPa) [38], Mg-3Zn-1Mn-0.5RGO (259.4 ± 8 MPa) [38], Mg-3Zn-1Mn-1.5RGO (231.5 ± 11 MPa) [38], Mg-1Al-Cu/0.18GNP (225 MPa) [54] and compact bone tissue (164–240 MPa) [55] which meet the specifications for orthopedic implant applications.

3.4. Machine learning-guided mechanical property correlations

Accurately predicting stress-strain curves for different amounts of BAGs can significantly streamline the material design process. Instead of conducting extensive physical experiments with every possible BAG amount, an accurate model can provide quick and reliable predictions, saving both time and resources. Therefore, advanced machine learning models such as LSTM, CNN, and GRU are explored for their potential in this context. The obtained comprehensive dataset (Fig. 5) forms the basis for training our regression models. A linear model serves as a baseline in this study. It assumes a direct proportionality between the input (strain) and the output (stress). While simple and computationally inexpensive, linear models often fail to capture complex data patterns, especially in nonlinear relationships. CNNs are primarily used for image recognition tasks but have shown promise in other areas, including time-series data. The key advantage of CNNs lies in their ability to automatically detect local patterns through convolutional layers, which can then be combined in deeper layers to form more complex features [26].

For this project, a 1D CNN was employed (Fig. 6(a)), which is suitable for time-series data. The CNN model

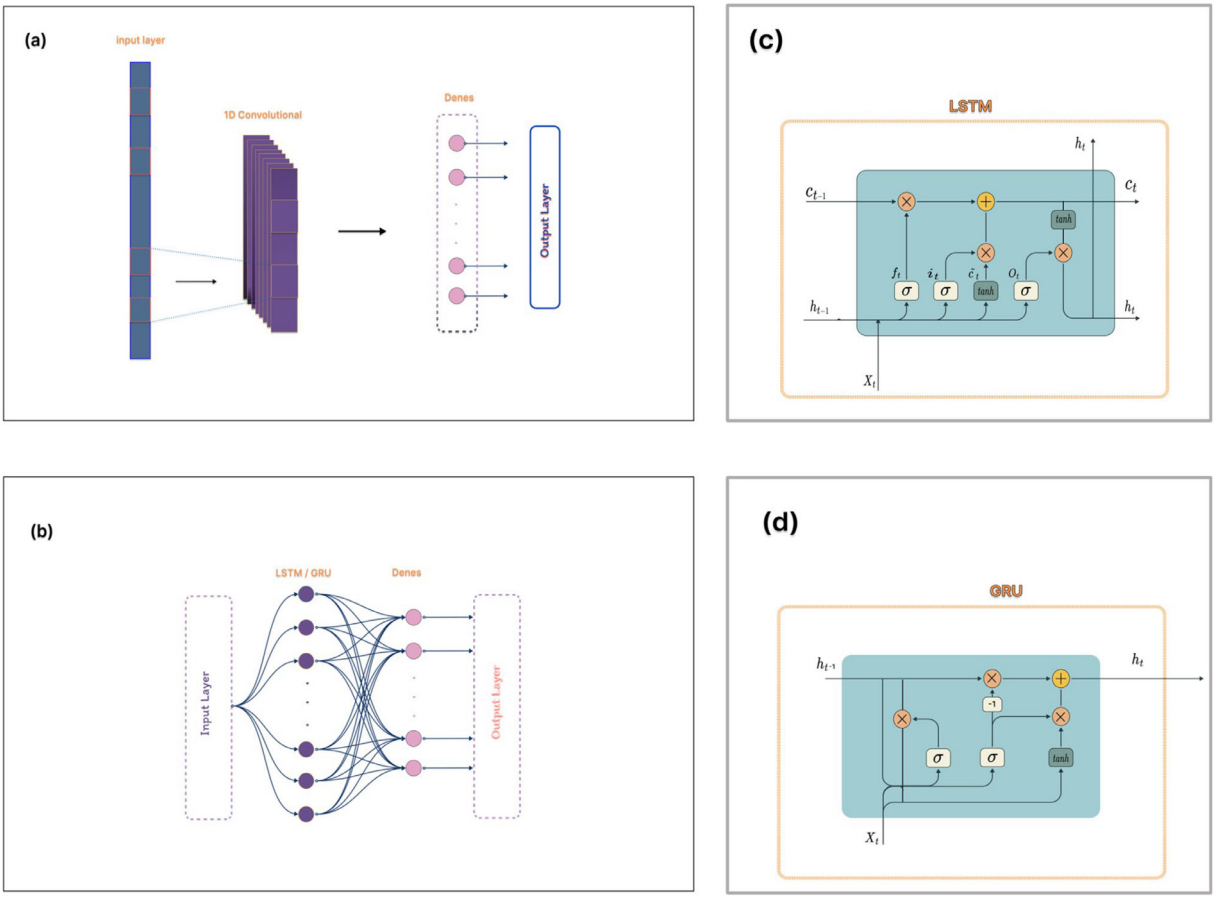

Fig. 6. The structure of (a) CNN network; (b) LSTM/GRU networks; (c) LSTM units; and (d) GRU units.

consists of a single convolutional layer with 64 filters and a kernel size of two. The convolutional layer processes the input sequence, identifying relevant patterns across small windows. The output is flattened, and two fully connected (dense) layers with 50 and 1 units, respectively, are used to refine the learned features and make predictions. The ReLU activation function is applied after each dense layer to introduce non-linearity, which is critical for modeling complex data. An LSTM learns long-term dependencies on data, which makes it suitable for time-series analysis [27]. There is a sequential nature to stress-strain relationships, although not strictly time-series data. LSTMs, with their gate mechanisms, can effectively manage the flow of information through long sequences, making them highly suitable for this application. The LSTM model in this paper consists of a single LSTM layer with 50 units, followed by two fully connected layers with 50 and 1 units, respectively (Fig. 6(b)). The ReLU activation function is applied to introduce non-linearities, enhancing the model's capability to approximate complex mappings between inputs and outputs. Compared to LSTMs, GRUs have fewer parameters (Fig. 6(c, d)), which can make training more efficient and less prone to overfitting, especially with smaller datasets. GRUs are a strong candidate for scenarios where model simplicity and training speed are critical [28]. The GRU model mirrors the structure of the LSTM, with one GRU layer comprising 50 units, followed by dense layers with 50 and 1 units, respectively (Fig. 6(b)). As with the CNN and LSTM models, ReLU activation functions were applied after the dense layers to model non-linear relationships in the data.

All models were implemented on a machine with these specifications: a Core i5–8250 U CPU, 8 GB of RAM, and running Windows 10 Pro. In addition to TensorFlow and Keras libraries, Python was used to develop the models. To prevent overfitting, the training was conducted with a batch size of 32. The Adam optimizer, known for its adaptive learning rate, was used for optimization, and Mean Squared Error (MSE) was employed as the loss function, given its relevance to continuous, numerical prediction tasks. To evaluate the models, three metrics were used:

- This is a measure of the average squared deviation between actual results and predicted results. Lower MSE values indicate better predictive accuracy.
- R-squared (R2) represents the proportion of dependent variables variance that can be predicted by the independent variables. An R2 score closer to 1 implies a better fit.
- A dimensionless measure of prediction accuracy is the NRMSE (Normalized Root Mean Square Error). This is the RMSE normalized by the range of observed values.

Please cite this article as: M. Ansari, S. Mahdavikia, H. Eslami et al., Fabrication and characterization of magnesium-based nanocomposites reinforced with Baghdadite and carbon nanotubes for orthopaedical applications, Journal of Magnesium and Alloys, https://doi.org/10.1016/j.jma.2024.12.004

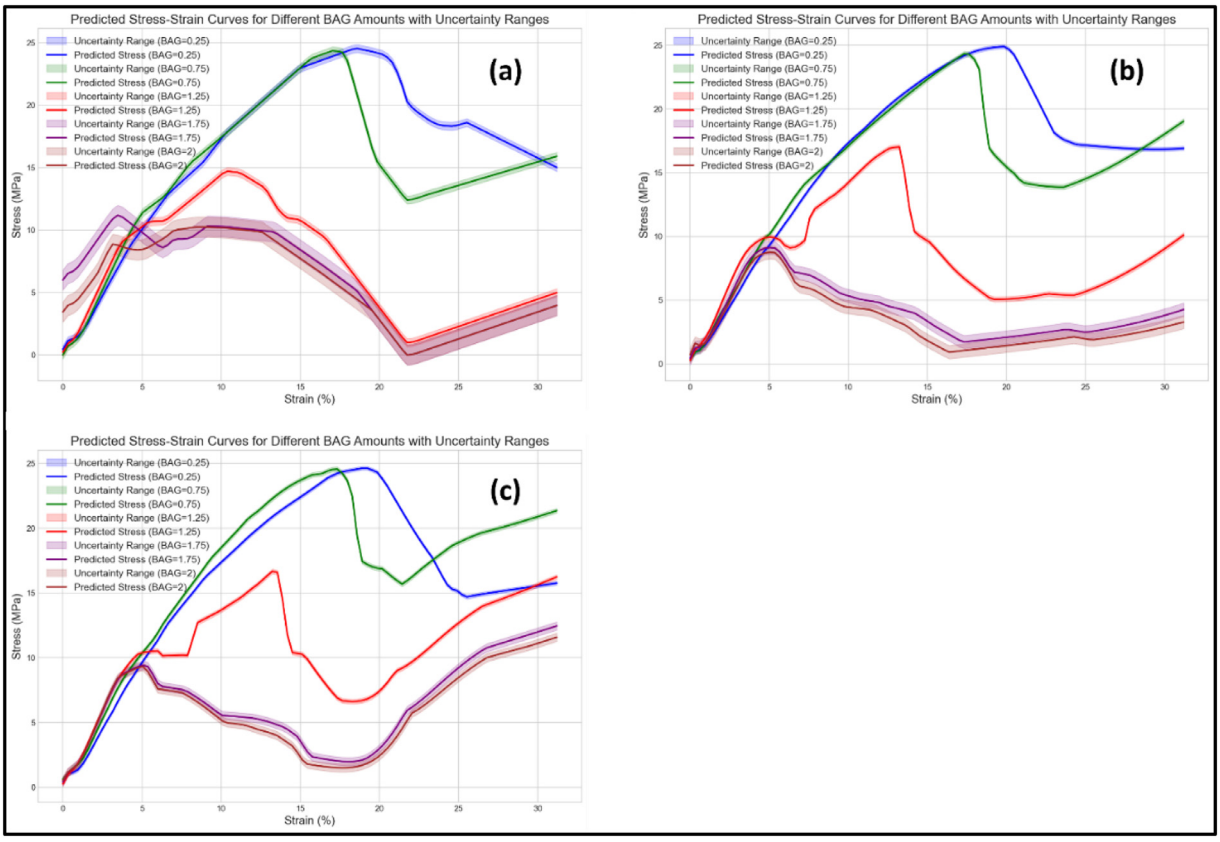

Fig. 7. The estimated Stress-Strain curves for unexperienced wt % of BAG using (a) CNN, (b) LSTM, and (c) GRU models.

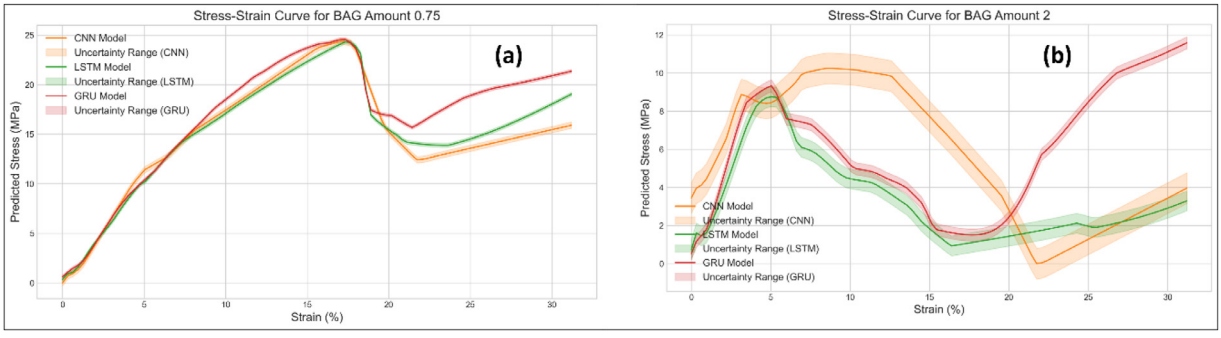

Fig. 8. Comparison of the predicted Stress-Strain curves using CNN, LSTM, and GRU models for (a) 0.75; (b) 2 wt.% BAG.

Fig. 7(a-c) indicate the estimated Stress-Strain curves for untested amounts of BAG (0.25 wt.%, 0.75 wt.%, 1.25 wt.%, 1.75 wt.%, and 2 wt%) using CNN, LSTM, and GRU models respectively. Both CNNs and recurrent models (LSTM, GRU) excel in identifying complex patterns and relationships in data compared to the CNN results, as it has been shown for 0.75 wt.% and 2 wt.% BAG (Fig. 8(a, b)). Advanced models can capture nonlinearities in the stress-strain relationship, providing more accurate predictions. Recurrent models are particularly adept at understanding the dependency of stress on previous strain values, leading to improved modeling of material behavior.

The results of our model evaluations are summarized in Fig. 9, which compares the R2 score and NRMSE for different models across the tested BAG amounts. The key observations are:

- The CNN model demonstrates strong performance with high R2 scores and low NRMSE values across all BAG amounts. The R2 scores are consistently above 0.9, indicating that the CNN model can explain over 90 % of the variance in the stress-strain data. The NRMSE values are also low, suggesting that the model predicts values that are close to reality. The slight decrease in performance as the BAG amount increases could be due to the increasing complexity of the stress-strain relationship with higher BAG content. Overall, the CNN model effectively captures the

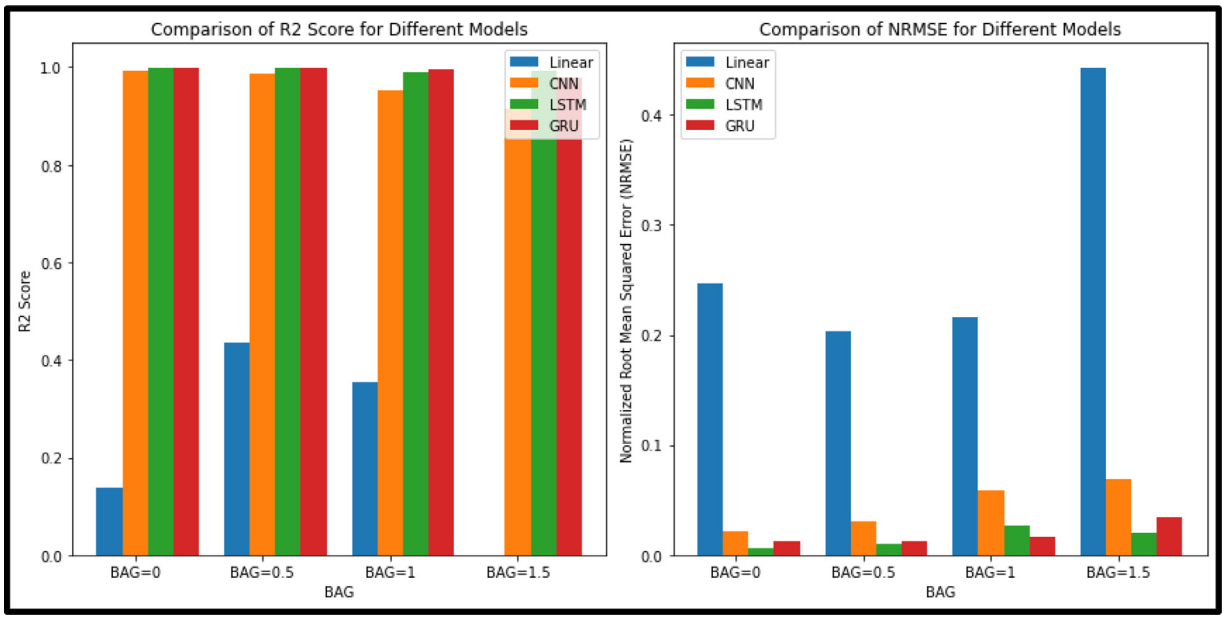

Fig. 9. Comparison of the NRMSE and R2 of tested Mg/CNTs/ wt.% BAG composites using the three non-linear regression models.

local patterns and features in the stress-strain data, making it a reliable choice for this task.

- The LSTM model outperforms the CNN model, achieving near-perfect R2 scores, especially for BAG amounts 0 % and 0.5 %, where the scores are almost 1. This indicates an exceptional fit to the data, with the model explaining virtually all the variance. The NRMSE values are also remarkably low, showing minimal deviation between the predicted and actual values. The LSTM model's superior performance can be attributed to its ability to capture long-term dependencies and temporal patterns in the sequential stress-strain data. This makes the LSTM model particularly effective for modeling the stress-strain behavior across different BAG amounts.
- The GRU model also exhibits excellent performance, with R2 scores close to one for all BAG amounts. These scores indicate that the GRU model can explain a significant portion of the variance in the stress-strain data. The NRMSE values are low, suggesting that the model's predictions are accurate and closely match the actual values. Although slightly lower than the LSTM model's performance, the GRU model's results are still highly impressive. The GRU's simpler architecture compared to the LSTM makes it computationally efficient while still effectively capturing the non-linear relationships in the stress-strain data.

Table 2 highlights the elastic region tilt (MPa/%) of stress-strain curves for measured and predicted data across varying BAG wt.%, showing that machine learning models (CNN, LSTM, GRU) effectively capture trends observed in measured data, such as higher stiffness at 0.5 wt.% BAG and reduced stiffness at 1 wt.% BAG. CNN predictions closely align with measured values, particularly for tested BAG amounts, while providing reasonable interpolations for untested BAG

Table 2
Tilt of the elastic region in stress-strain curves (MPa/%) for measured data and predicted curves (CNN, LSTM, GRU) across varying wt.% BAG, including untested BAG amounts.

wt.% Bag	Type of the Curve	Predicted curve
0	Measured data	1.74573
1	Measured data	1.395147
0.5	Measured data	2.084508
1	Measured data	0.105642
0	CNN estimate	1.823532
0.5	CNN estimate	1.39551
1	CNN estimate	2.072484
1.5	CNN estimate	0.109362
0.25	CNN estimate	1.511344
0.75	CNN estimate	1.924291
1.25	CNN estimate	0.043392
1.75	CNN estimate	0.174584
2	CNN estimate	0.03992
0	LSTM estimate	1.716112
0.5	LSTM estimate	1.377428
1	LSTM estimate	2.075913
1.5	LSTM estimate	0.107607
0.25	LSTM estimate	1.511061
0.75	LSTM estimate	1.907036
1.25	LSTM estimate	2.121342
1.75	LSTM estimate	0.028851
2	LSTM estimate	0.0149
0	GRU estimate	1.737
0.5	GRU estimate	1.39718
1	GRU estimate	2.079168
1.5	GRU estimate	0.104969
0.25	GRU estimate	1.420866
0.75	GRU estimate	1.543862
1.25	GRU estimate	2.051309
1.75	GRU estimate	0.036426
2	GRU estimate	0.005569

Please cite this article as: M. Ansari, S. Mahdavikia, H. Eslami et al., Fabrication and characterization of magnesium-based nanocomposites reinforced with Baghdadite and carbon nanotubes for orthopaedical applications, Journal of Magnesium and Alloys, https://doi.org/10.1016/j.jma.2024.12.004

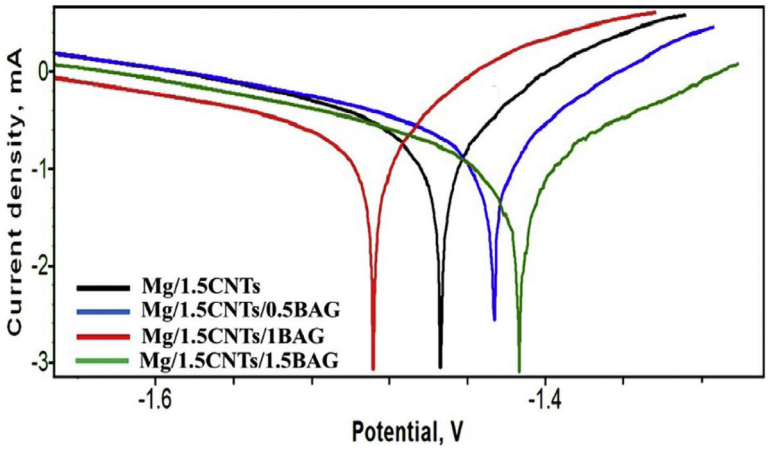

Fig. 10. Potentiodynamic polarization curves of Mg/CNTs/BAG composites containing different amounts of Baghdadite in a body-simulating environment at 37 °C.

levels, with decreasing tilt observed at higher BAG contents (e.g., 1.75 wt.% and 2 wt.%). LSTM demonstrates superior consistency with measured data across tested and untested BAG amounts, capturing nonlinearities in stiffness, whereas GRU predictions, while accurate for lower BAG levels, show slightly less precision at higher contents, emphasizing model differences in capturing BAG-related stiffness changes. These findings emphasize the importance of choosing advanced machine learning models for accurately predicting composite materials' mechanical properties.

3.5. In-vitro corrosion behavior of Mg/CNTs/BAG composites

Fig. 10 illustrates the potential polarization curves for the Mg/CNTs alloy and Mg/CNTs/BAG composites containing 0.5–1.5 wt.% BAG, recorded after 30 min of immersion in SBF. Using Tafel fits of the polarization curves, corrosion potential (E_{corr}) and corrosion current density (i_{corr}) were determined and analyzed with Powersuite software. The results in Fig. 10 reveal that, in comparison with Mg/CNTs alloy, the Mg/CNTs/BAG composites exhibit significantly suppressed anodic currents. Additionally, the corrosion potential shifted to more negative values with the addition of 0.5 and 1.5 wt.% BAG. This indicates enhanced resistance to corrosion, highlighting the superior corrosion inhibition provided by BAG reinforcement in composites [54]. As shown in Table S3 in the supporting information, the corrosion potentials for Mg/CNTs alloy, Mg/CNTs–0.5BAG, Mg/CNTs–1.0BAG and Mg/CNTs–1.5BAG were evaluated as −1.48, −1.43, −1.55, and −1.4 V, respectively. It is generally accepted that both thermodynamic and kinetic corrosion benefit from lower E_{corr} and higher E_{corr} values [55]. Table S3 shows corrosion current densities for Mg/CNTs alloy, Mg/CNTs–0.5BAG, Mg/CNTs–1.0BAG, and Mg/CNTs–1.5BAG were assessed as 398, 276, 398, and 135 μA, respectively. As will be shown in the following sections and Table S3, it is evident that the corrosion current density for Mg/CNTs was 398 A, which decreased to 135 A when the BAG contents were added to the composite up to 1.5 wt.%. This is attributed to decreased surface roughness [56] and hydrophilicity (48° ± 3°) of the composite. When 1.5 wt.% BAG was present, corrosion potential decreased (Fig. 12(e) and Table S3). As a result, the addition of BAG contents to the composite decreased crack formation during micro-galvanic degradation and crevice corrosion [57,58]. As a result, the CR of these specimens was improved over the CR of the uncoated Mg/CNT alloy (Fig. 12(e)). Likewise, the high BAG contents of Mg/CNTs-1.5BAG composites experienced a lower slope of the anodic branch (βa) in the polarization curves compared to the Mg/CNTs alloy, as follows: Mg/CNTs–1.5BAG (101 mV/decade) < Mg/CNTs–1.0BAG (199 mV/decade) > Mg/CNTs-0.5BAG (117 mV/decade) < Mg/CNTs alloy (150 mV/decade). On the one hand, the anode curve showed a current plateau at a low anode potential indicating the potential for dispersed BAGs to improve the corrosion resistance (CR) of Mg matrices due to the formation of excellent passivation layers of Mg/CNTs/BAG composites. On the other hand, the lowest value in the ICORR and βa demonstrates the synergistic effects of the BAG contents to lower the DCR of Mg/CNTs/BAG films as a result of the absence of secondary phases (such as Mg2Ca intermetallic phase) and its intensive role in micro-galvanic corrosion of the Mg alloys at their grain boundaries [16,32,59–67]. These results are complemented by water contact angle (WCA) data obtained from the composites that were fabricated [62].

A corrosion resistance study of Mg/CNTs alloys and Mg/CNTs/BAG films was conducted in further detail by EIS in SBF at 37 °C. Fig. 11(a) illustrates a Nyquist plot comparing the composite film with the Mg/CNT alloy. Typical EIS spectra of Mg/CNT alloys have three different time constants (Fig. 11(a)). High frequency is related to an interfacial capacitance in conjunction with the charge transfer resistance. The relaxation of the adsorbed precursors is attributed to the lower frequency induction loop, while the time constant at intermediate frequencies is explained by the diffusion of Mg+2 ions inside the porous layer of corrosion products [63]. Mg/CNTs/BAG composites exhibited a complete semicircle loop at high frequencies (capacitive loop) and an

Please cite this article as: M. Ansari, S. Mahdavikia, H. Eslami et al., Fabrication and characterization of magnesium-based nanocomposites reinforced with Baghdadite and carbon nanotubes for orthopaedical applications, Journal of Magnesium and Alloys, https://doi.org/10.1016/j.jma.2024.12.004

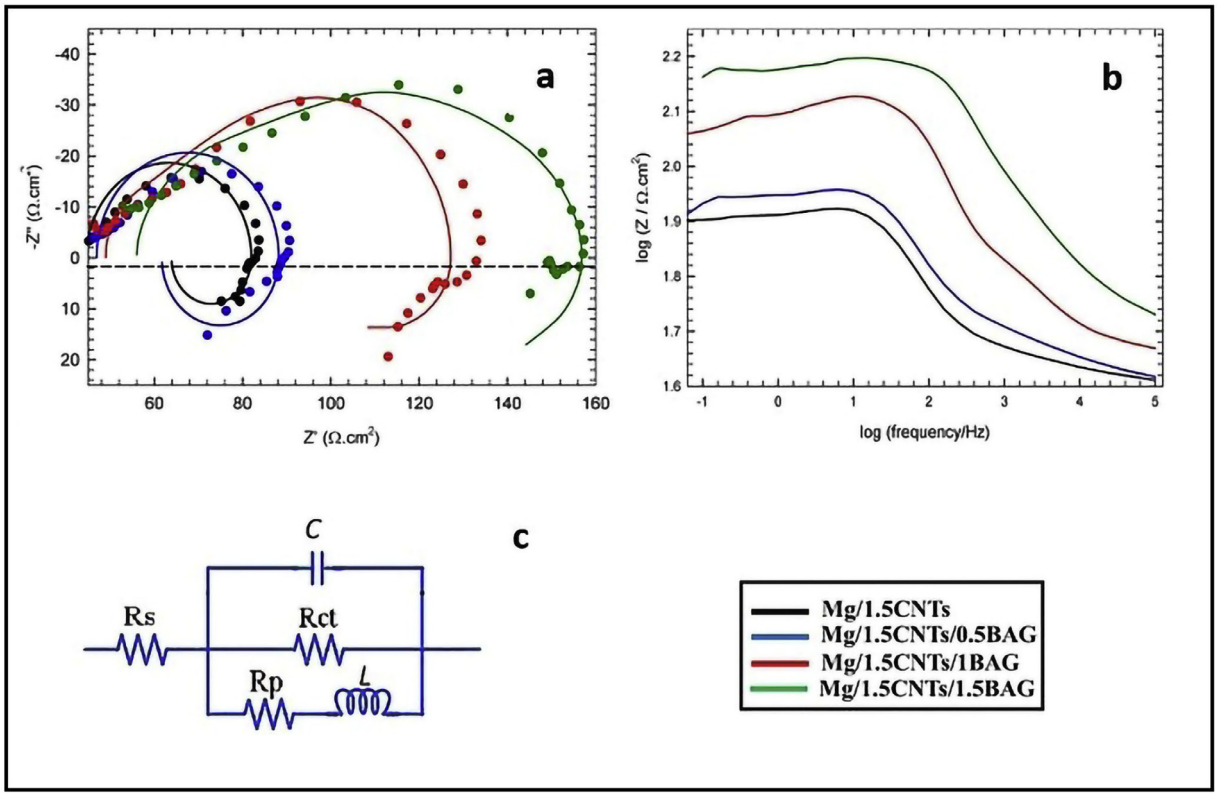

Fig. 11. (a, and b) Nyquist and Bad-Z curves of Mg/CNTs/BAG composites containing different amounts of Baghdadite in a body simulator environment at 37 °C and (C) the drawn equivalent circuit Based on the EIS curves for the samples.

inductive loop at low frequencies (inductive loop). As the size of the high-frequency capacitor loop expanded, the CR of the films increased. As evidenced by the high-frequency capacitor resistance arc, the electrochemical reaction occurred at the interface between the Mg/CNTs/BAG films and the corrosive medium. Accordingly, charge transfer governed the electrochemical reaction in the system rather than the dissolution/dissolution rate of magnesium [HT1]. A greater capacitive arc radius is generally associated with excellent CR in Nyquist plots [32]. It was evident that the Mg/CNTs–1.5BAG composite had the largest arc radius, confirming its excellent corrosion resistance during its corrosion examination, establishing it as an appropriate implant candidate. In order to evaluate the EIS spectra of Mg/CNTs/BAG composites reinforced with BAG contents further, an equivalent electrical circuit model (Fig. 11(b)) was created, and fitting lines are depicted in Fig. 11(a). According to this model, C and Rct represent double-layer capacitance and charge transfer resistance, respectively, while Rs represents electrolyte resistance, Rp represents polarization resistance, and L represents the inductor capacity. As described in the supporting information, Table S4 provides the derived kinetic parameters. Because of its strong charge transfer resistance, the sample is generally resistant to corrosion. As a result, the charge transfer resistance (R_{ct}) of Mg/1.5CNTs jumped to 49.10 cm^2 in Mg/CNTs-1.5BAG, which is consistent with the results obtained during the polarization tests. In order to enhance the protection of the Mg/CNT matrix, a protective layer of calcium silicate was formed on the active surface of SBF as a result of the composition of Mg/CNTs with BAGs. Furthermore, grain refinement reduces the mismatch-induced stress between the surface layer and the Mg substrate, thereby preventing corrosion pits from forming. As carbon nanotubes form a natural diffusive barrier between the protected metal and reactants, they are suitable materials for barrier layers to prevent corrosion. As a result, the accumulated SBF solution is gradually prevented from entering the Mg surface and, as a result, the DCR is reduced and the corrosion resistance (CR) of the Mg alloy is increased [20,64]. The Bode diagrams for the various samples are shown in Fig. 11(c). A higher CR is indicated by a greater impedance modulus at lower frequencies ($|Z|$ $f = 0.1$ Hz). For the Mg/CNTs alloy substrates, the impedance modulus was only 1 Ω·cm^2, whereas those of the Mg/CNTs-0.5BAG, Mg/CNTs-1.0BAG and Mg/CNTs-1.5BAG samples increased to 1, 2, and 3 k Ω·cm^2, respectively implying that the physical barrier effect of the composite film was gradually enhanced.

3.6. Cytotoxicity assessment and cell response of Mg/CNTs-(0.5–1.5 wt.%) BAG composites

After the implantation of magnesium-based biomaterials (MBs), it is essential to create and preserve a mature bone interface between the implant and bone [1]. A vital stage in the process is cell attachment to orthopedic implants, a process mostly mediated by Integrin receptors, which are

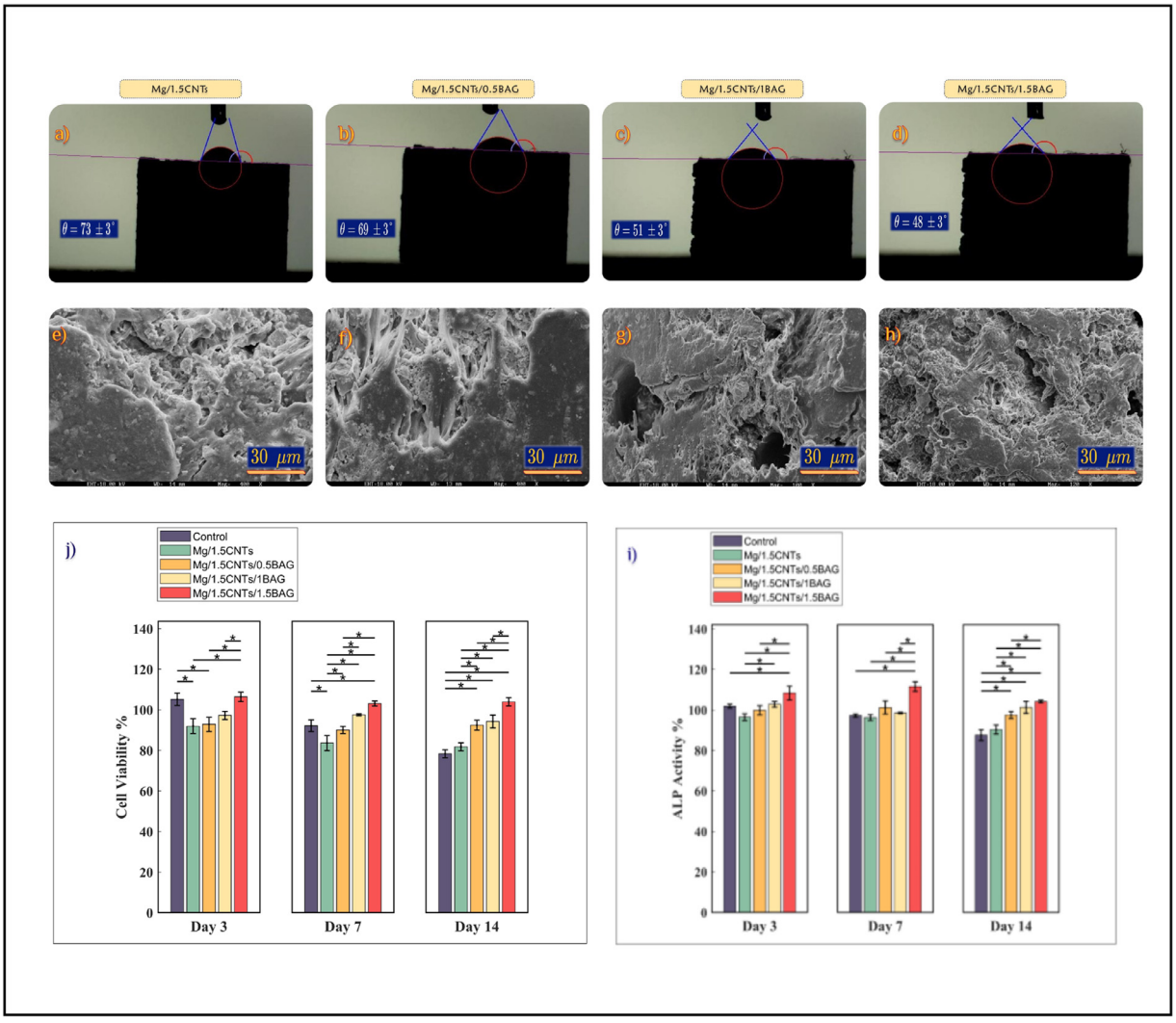

Fig. 12. (a-d) Static Water Contact Angles for Mg/CNTs/xBAG (x = 0, 0.5, 1 and 1.5 wt%) nanocomposites synthesized with SPS (50 MPa pressure and 450 °C temperature); (e-h) SEM images of the morphology and adhesion of AD-MSCs after 14 days; (i) Viability and proliferation of MG-63 cells and (j) ALP activity of AD-MSCs cultured for various times.

transmembrane adhesion proteins that link the interior of cells to the extracellular environment [53]. MTT assay was used further to assess the cytotoxicity profile of such composite-based scaffolds and demonstrate their potential in terms of cellular attachment, migration, and proliferation [59,31]. Previous studies have shown that the hydrophilic nature of scaffolds has a beneficial impact in terms of their cellular attachment and proliferation [32,65,66]. The Static Water Contact Angles (SWCA) on Mg/1.5CNTs/BAG composites of different BAG contents were calculated in order to determine their hydrophilic characteristics, as shown in Fig. 11(a). As expected, the SWCA of Mg/1.5CNTs alloy was 73° ± 5°, which was mainly due to an inherent hydrophobic property of the agglomerated CNTs of 1.5 wt.% overwhelmed by more hydrophilic sites within the Mg matrix [57]. The hydrophilic property of the Mg/1.5CNTs/BAG composites was significantly improved with the introduction of BAGs [58]. The hydrophilic property of the Mg/1.5CNTs/BAG composites was significantly improved with the introduction of BAGs. The water contact angle of Mg/CNTs-0.5BAG, Mg/CNTs-1.0BAG and Mg/CNTs-1.5BAG were 61° ± 4°, 51° ± 3° and 48° ± 3°, respectively. Because SWCA at 0° to 90° shows hydrophilicity [56]. Due to the presence of silanol (Si-OH) functional groups in BAG content, all composite specimens have hydrophilic surfaces. Fig. 12(e-h) is a series of SEM images of specimens after immersion in DMEM + 10 % FBS for 72 h. These micrographs show that the surface of the Mg/CNTs alloy and Mg/CNTs/BAG composites were pitted, and that pitting became less extensive and more infinitesimal with increasing the BAG contents during loner immersion time. The corrosion morphology remained similar on the entire alloy and composites surfaces after immersion of 72 h, except for the Mg/CNTs–1.0BAG composite where a completely different morphology could be noticed in Fig. 12(g). The viability of the cell cultured on both Mg/CNTs alloy and Mg/CNTs/BAG composites was assessed using MTT assay, with the cell proliferation on the TCP plate being the control as depicted in Fig. 12(i). The result of MTT assay

Please cite this article as: M. Ansari, S. Mahdavikia, H. Eslami et al., Fabrication and characterization of magnesium-based nanocomposites reinforced with Baghdadite and carbon nanotubes for orthopaedical applications, Journal of Magnesium and Alloys, https://doi.org/10.1016/j.jma.2024.12.004

demonstrated the highest increase in cell proliferation in cultured composite groups compared to the TCP group over the long times. In particular, the cell proliferation of the composites amplified with the expansion of culture time and increased up to day 3 in all groups. The MTT results showed a significant increase of cell proliferation at concentrations ranging from 0.5 wt% to 1.5 wt% BAGs. In day 3, it was higher in Mg/CNTs-1.5BAG than Mg/CNTs and TCP groups (p value$<$0.05).

One of the most significant early osteogenic commitment determinants is ALP activity. It is an osteoblast cell biochemical marker that is crucial for bone mineralization and differentiation [46,67,68]. The ALP activity was measured after 3, 7, and 14 days of cell culturing. As demonstrated in Fig. 12(j), increase activity of ALP was significant on day 14 compared to cells on day 3 and 7 (p value$<$ 0.05). In the four groups, ALP on days 3, 7, and 14 was peaked in Mg/CNTs/BAG composite groups (p value$<$ 0.05). On day 14, the highest amount of ALP activity was observed in Mg/CNTs/1.5BAG group.

4. Conclusion

The SPS method was successfully implemented to prepare dense nanocomposites of a light-weight metal alloy (magnesium-1.5 wt.% carbon nanotubes) reinforced and composited with synthesized baghdadite (Ca3ZrSi2O9) in The various weight fractions (0.5–1.5 wt.%) and their microstructure, mechanical robustness, degradation properties, and cytotoxicity were investigated by a broad variety of microscopic, analytical, and mechanical techniques, machine learning analyses, and direct in vitro assay in SBF for 3 weeks. The BAG contents reduced the degradation rates of Mg/CNTs/BAG composites. Mg/CNTs-1.5BAG had Ecorr and icorr equal to -1396 mV and 135 μA, respectively which was an indication of the improvement in the CR. The microstructure, dimensions, area, volume, and mass of magnesium composites influenced their in vitro degradation properties, including their degradation rates and modes, under consistent conditions of degradation. The BAG contents enhanced the micro hardness of Mg/CNTs/BAG composites. The microhardness of the Mg/CNTs-1.5BAG composite reached $\sim$83.00 HV. The failure strain and CS showed a similar pattern. Additionally, Mg/CNTs-0.5BAG maintains a compressive strength of 259.75 MPa, which still satisfies the mechanical specifications for load-bearing implants. Machine learning models—CNN, LSTM, and GRU—leveraged to predict stress-strain relationships for magnesium composites with varying BAG amounts, reducing the reliance on time-intensive physical experiments. The results demonstrated the significant advantages of these advanced models over traditional linear methods, with LSTM and GRU achieving near-perfect R^2 scores and low NRMSE values, effectively capturing the nonlinear and sequential dependencies in the data. The CNN model also showcased strong performance, particularly in identifying localized patterns within the stress-strain data. These findings underscore the potential of machine learning to revolutionize material design by enabling accurate, resource-efficient predictions of mechanical properties. Mg/CNT-1.5BAG significantly increased the average FBS adhesion density and cell proliferation under indirect contact in 72-hour indirect cultures with FBS, as compared to non-composited Mg/CNT. Due to its lower corrosion rate when baghdadite is distributed properly, the composite exhibited better cytocompatibility than the Mg/CNT alloy. A protective surface layer is formed as a result of the good distribution of baghdadite. Additionally, MATLAB-based image analysis of SEM particle sizes reveals unimodal distributions across all samples in the histograms. The surface chemistry, microstructure, and morphology of CNT and BAG contents in Mg-based composites may significantly influence FBS adhesion, morphology, and subsequence cell viabilities under direct contact. However, FBS adhesion and morphology were primarily determined by the dynamics of concentration gradient surrounding the Mg-based composites and the release of soluble degradation products from a degraded sample under indirect contact. In conclusion, Mg-based biodegradable composites containing CNTs, and BAGs appear promising for load-bearing implant applications and should be further investigated in vivo for clinical applications.

Declaration of Competing Interest

The authors declare that they have no known competing financial interests or personal relationships that could have appeared to influence the work reported in this paper.

Supplementary materials

Supplementary material associated with this article can be found, in the online version, at doi:10.1016/j.jma.2024.12.004.

CRediT authorship contribution statement

Mojtaba Ansari: Writing – review & editing, Writing – original draft, Visualization, Validation, Supervision, Methodology, Investigation, Formal analysis, Data curation, Conceptualization. **Shiva Mahdavikia:** Writing – original draft, Formal analysis, Data curation, Conceptualization. **Hossein Eslami:** Supervision, Resources. **Mozhdeh Saghalaini:** Writing – review & editing, Writing – original draft, Software, Investigation. **Hamid Taghipour:** Writing – review & editing, Writing – original draft. **Fatemeh Zare:** Writing – review & editing, Writing – original draft, Resources. **Shahin Shirani:** Writing – review & editing, Writing – original draft. **Mohammad Hossein Alizadeh Roknabadi:** Writing – review & editing, Writing – original draft, Visualization, Validation, Software, Resources, Project administration, Investigation, Data curation, Conceptualization.

References

[1] H. Zhou, B. Liang, H. Jiang, Z. Deng, K. Yu, J Magnes Alloys 9 (3) (2021) 779–804, doi:10.1016/j.jma.2021.03.004.

Please cite this article as: M. Ansari, S. Mahdavikia, H. Eslami et al., Fabrication and characterization of magnesium-based nanocomposites reinforced with Baghdadite and carbon nanotubes for orthopaedical applications, Journal of Magnesium and Alloys, https://doi.org/10.1016/j.jma.2024.12.004

[2] V.K. Bommala, M.G. Krishna, C.T. Rao, J Magnes Alloys 7 (1) (2019) 72–79, doi:10.1016/j.jma.2018.11.001.
[3] F. Witte, V. Kaese, H. Haferkamp, E. Switzer, A. Meyer-Lindenberg, C.J. Wirth, H. Windhagen, Biomaterials 26 (17) (2005) 3557–3563, doi:10.1016/j.biomaterials.2004.09.049.
[4] N.G. Atia, H.R. Barai, H.K. Shalaby, N.G. Ali, S.M. Morsy, M.M. Ghobashy, H.A. Attia, S.W. Joo, ACS Omega 7 (49) (2022) 44532–44541, doi:10.1021/acsomega.2c05596.
[5] A. Feng, Y. Han, Mater Des 32 (5) (2011) 2813–2820.
[6] A. Dubey, S. Jaiswal, D. Lahiri, J Mater Eng Perform 28 (2) (2019) 800–809.
[7] S. Jaiswal, R. Kumar, P. Gupta, M. Kumaraswamy, P. Roy, D. Lahiri, J Mech Behav Biomed Mater 78 (2018) 442–454.
[8] I. Nakahata, Y. Tsutsumi, E. Kobayashi, Metals (Basel) 10 (10) (2020) 1314.
[9] S.N. Dezfuli, S. Leeflang, Z. Huan, J. Chang, J. Zhou, Materials Science and Engineering C 79 (2017) 647–660.
[10] Z. Huan, M. Leeflang, J. Zhou, J. Duszczyk, Mater Sci Eng: B 176 (20) (2011) 1644–1652.
[11] S. Dutta, K. Devi, S. Mandal, et al., Materialia (Oxf) 5 (2019) 100245.
[12] C. Shuai, B. Wang, S. Bin, S. Peng, C. Gao, Mater Des (2020) 108612.
[13] L.Z. Wang, W.H. Wei, Int J Mater Res 18 (3) (2017) 192–201.
[14] S. Abazari, A. Shamsipur, H.R. Bakhsheshi-Rad, A.F. Ismail, S. Sharif, M. Razzaghi, S. Ramakrishna, F Berto, Materials (Basel) 13 (19) (2020) 4421, doi:10.3390/ma13194421.
[15] J. Williams, W. Broughton, T. Koukoulas, S.S. Rahatekar, J Mater Sci 48 (3) (2013) 1005–1013, doi:10.1007/s10853-012-6830-3.
[16] M. Yang, L. Zhang, Q. Shen, Synthesis and sintering of mg2si thermoelectric generator by spark plasma sintering, J Wuhan Uni Technol-Mat Sci, 23, 2008, pp. 870–873, doi:10.1007/s11595-007-6870-8.
[17] Z. Karimi, E. Seyedjafari, F.S. Mahdavi, S.M. Hashemi, A. Khojasteh, B. Kazemi, S. Mohammadi-Yeganeh, J Biomed Mater Res Part A 2019 (107A) (2019) 1284–1293.
[18] H. Fukuda, J.A. Szpunar, K. Kondoh, R. Chromik, Corros Sci 52 (12) (2010) 3917–3923.
[19] W.N.A.W. Muhammad, Y. Mutoh, Y. Miyashita, Adv Mat Res 129 (2010) 764–768.
[20] Z.A. Munir, U. Anselmi-Tamburini, M. Hyanagi, J Mater Sci 41 (3) (2010) 763–777.
[21] I. Ahmad, M. Islam, T. Subhani, Y. Zhu, Nanotechnology 27 (42) (2016) 425704, doi:10.1088/0957-4484/27/42/425704.
[22] A.E. Rodríguez-Sánchez, Neural Comput Applic 36 (2024) 20687–20697, doi:10.1007/s00521-024-10320-0.
[23] S. Sadeghzade, R. Emadi, T. Ahmadi, F. Tavangarian, Mater Chem Phys 228 (2019) 89–97.
[24] M.A. Sainz, S. Serena, A. Caballero, Ceram Int 49 (12) (2023) 19569–19577.
[25] International Organization for Standardization. (2014). . https://www.iso.org/standard/51257.html
[26] Y. LeCun, Y. Bengio, G. Hinton, Nature 521 (7553) (2015) 436–444, doi:10.1038/nature14539.
[27] S. Hochreiter, J. Schmidhuber, Neural Comput 9 (8) (1997) 1735–1780, doi:10.1162/neco.1997.9.8.1735.
[28] Cho, K., Van Merrienboer, B., Gulcehre, C., Bahdanau, D., Bougares, F., Schwenk, H., & Bengio, Y. (2014). . ArXiv./abs/1406.1078
[29] P. Thangaraju, S.B. Varthya, in: ISO 10993: biological evaluation of medical devices. medical device guidelines and regulations handbook, Springer, 2022, pp. 163–187. https://nhiso.com/wp-content/uploads/2018/05/ISO-10993-1-2009.pdf. Available:.
[30] Z. Karimi, E. Seyedjafari, F.S. Mahdavi, S.M. Hashemi, A. Khojasteh, B. Kazemi, S. Mohammadi-Yeganeh, J Biomed Mater Res Part A 2019 (107A) (2019) 1284–1293.
[31] L. Pan, X. Pei, R. He, Q. Wan, J. Wang, Colloids and Surfaces B: Biointerfaces 93 (2012) 226–234, doi:10.1016/j.colsurfb.2012.01.011.
[32] S. Abazari, A. Shamsipur, H.R. Bakhsheshi-Rad, J Magnes Alloys 10 (12) (2022) 3612–3627, doi:10.1016/j.jma.2021.09.016.
[33] J. Williams, W. Broughton, T. Koukoulas, S.S. Rahatekar, J Mater Sci 48 (3) (2013) 1005–1013, doi:10.1007/s10853-012-6830-3.
[34] S. Mehrafzoon, S. Hassanzadeh-Tabrizi, A. Bigham, Ceram Int 44 (12) (2018) 13951–13958, doi:10.1016/j.ceramint.2018.04.244.
[35] S. Sadeghzade, F. Shamoradi, R. Emadi, F. Tavangarian, J Mech Behav Biomed Mater 68 (2017) 1–7, doi:10.1016/j.jmbbm.2017.01.034.
[36] L. Nikzada, R. Licheri, T. Ebadzadeh, R. Orru, G. Cao, Ceram Int 38 (8) (2012) 6469–6480.
[37] J. Xu, Y. Zhang, Z. Li, Y. Ding, X. Zhao, X. Zhang, H. Wang, C. Liu, X. Guo, Nanomaterials 12 (24) (2022) 4446, doi:10.3390/nano12244446.
[38] G. Balakrishnan, R. Velavan, K.M. Batoo, E.H. Raslan, Results in Physics 16 (2020) 103013, doi:10.1016/j.rinp.2020.103013.
[39] M.E. Birch, T. A, M. Chai, R. Andrews, R.L Hatfield, Ann Occup Hyg 57 (9) (2013) 1148–1166, doi:10.1093/annhyg/met042.
[40] D. Garbiec, F. Heyduk, B. Pachutko, D. Andrezejeweski, Metal forming 45 (3) (2016) 263–272.
[41] K. Munir, C. Wen, Y. Li, J Magnes Alloys 8 (1) (2020) 269–290, doi:10.1016/j.jma.2019.12.002.
[42] W. Xia, G. Dehm, S. Brinckmann, J Mater Sci 55 (2020) 9095–9108, doi:10.1007/s10853-020-04646-y.
[43] A. Mandal, P. Modak, M. Sen, et al., J Mater Sci 57 (2022) 1390–1402, doi:10.1007/s10853-021-06605-7.
[44] J. Fan, J. Li, Z. Huang, P.H. Wen, C.G. Bailey, Computat Mater Sci 144 (2018) 113–119, doi:10.1016/j.commatsci.2017.12.017.
[45] M. Rahman, Y. Li, C. Wen, J Magnes Alloys 8 (3) (2020) 929–943, doi:10.1016/j.jma.2020.05.003.
[46] T.C. Schumacher, A. Aminian, E. Volkmann, H. Lührs, D. Zimnik, D. Pede, W. Wosniok, L. Treccani, K. Rezwan, Biomed Mater 10 (5) (2015) 055013, doi:10.1088/1748-6041/10/5/055013.
[47] E. Aguilar, Biomed Mater Devices (2021), doi:10.1016/j.ceramint.2021.02.178.
[48] S. Yadav, S. Majumdar, A. Ali, S. Krishnamurthy, P. Singh, R. Pyare, Ceram Int 47 (11) (2021) 16037–16053, doi:10.1016/j.ceramint.2021.02.178.
[49] M. Wang, Y. Zhao, L.-D. Wang, Y.-P. Zhu, X.-J. Wang, J. Sheng, Z.-Y. Yang, H.-L. Shi, Z.-D. Shi, W.-D. Fei, Carbon N Y 139 (2018) 954–963, doi:10.1016/j.carbon.2018.08.009.
[50] M. Rashad, F. Pan, A. Tang, M. Asif, M. Aamir, J Alloys Compd 603 (2014) 111–118, doi:10.1016/j.jallcom.2014.03.038.
[51] Huanran Lin, Xiuhua Guo, Kexing Song, Jiang Feng, Shaolin Li, Xiangfeng Zhang, Nanotechnol Rev 10 (1) (2021) 62–72, doi:10.1515/ntrev-2021-0006.
[52] Y. Say, O. Guler, B. Dikici, Mater Sci Eng: A 798 (2020) 13936.
[53] M. Shahin, K. Munir, C. Wen, Y. Li, J Alloys Compd 828 (2020) 154461, doi:10.1016/j.jallcom.2020.154461.
[54] N. Safari, N. Golafshan, M. Kharaziha, M.R. Toroghinejad, L. Utomo, J. Malda, M. Castilho, ACS Biomater Sci Eng (2020), doi:10.1021/acsbiomaterials.0c00613.
[55] F. Witte, N. Hort, C. Vogt, S. Cohen, K.U. Kainer, R. Willumeit, F. Feyerabend, Curr Opin Solid State Mater Sci 12 (5–6) (2008) 63–72, doi:10.1016/j.cossms.2009.04.001.
[56] A.M.A. Mohamed, A.M. Abdullah, N.A. Younan, Arabian J Chemist 8 (6) (2015) 749–765, doi:10.1016/j.arabjc.2014.03.006.
[57] M. Shahin, C. Wen, K. Munir, Y. Li, J Magnes Alloys 10 (2) (2022) 458–477, doi:10.1016/j.jma.2021.05.011.
[58] F. Soleymani, R. Emadi, S. Sadeghzade, F. Tavangarian, Coatings. 9 (12) (2019) 789, doi:10.3390/coatings9120789.
[59] Z. Shao, P. Li, C. Zhang, B. Wu, C. Tang, M. Gao, J Magnes Alloys 12 (6) (2024) 2520–2533, doi:10.1016/j.jma.2022.10.014.
[60] R. Wang, D. Wang, H. Nagaumi, Z. Wu, X. Li, H. Zhang, Corros Sci (2022) 110468, doi:10.1016/j.corsci.2022.110468.
[61] M.C. Lopes de Oliveira, R.M. Pereira da Silva, R.M. Souto, R.A. Antunes, J Magnes Alloys 10 (11) (2022) 2997–3030, doi:10.1016/j.jma.2022.09.024.
[62] Z.-Y. Ding, L.-Y. Cui, X.-B. Chen, R.-C. Zeng, S.-K. Guan, S.-Q. Li, F. Zhang, Y.-H. Zou, Q.-Y. Liu, J Alloys Compd 764 (2018) 250–260, doi:10.1016/j.jallcom.2018.06.073.
[63] D.S.S. Almeida, D.D. dos Santos, N.B.G. Ferreira, C.Q. Correia, B.C. Gomes, E.A. Ferreira, L.P. Moreira, J.A. de Castro,

J.A.O. Huguenin, L. da Silva, J Mater Res Technol 9 (5) (2020) 10175–10183, doi:10.1016/j.jmrt.2020.07.030.

[64] J.-X. Tao, M.-C. Zhao, Y.-C. Zhao, D.-F. Yin, L. Liu, C. Gao, C. Shuai, A. Atrens, J Magnes Alloys 8 (3) (2020) 952–962, doi:10.1016/j.jma.2019.10.004.

[65] C. Shuai, Z. Zeng, Y. Yang, F. Qi, S. Peng, W. Yang, C. He, G. Wang, G. Qian, Mater Des 190 (2020) 108564, doi:10.1016/j.matdes.2020.108564.

[66] C. Shuai, G. Liu, Y. Yang, F. Qi, S. Peng, W. Yang, Z. Liu, Ceram Int 45 (16) (2019) 20234–20242, doi:10.1016/j.ceramint.2019.06.296.

[67] L.T. De Jonge, J.J. Van den Beucken, S.C. Leeuwenburgh, A.A. Hamers, J.G. Wolke, J.A. Jansen, Acta Biomater 5 (7) (2009) 2773–2782, doi:10.1016/j.actbio.2009.03.019.

[68] H. Zreiqat, Y. Ramaswamy, C. Wu, A. Paschalidis, Z. Lu, B. James, O. Birke, M. McDonald, D. Little, C.R. Dunstan, Biomaterials 31 (12) (2010) 3175–3184, doi:10.1016/j.biomaterials.2010.01.024.

Please cite this article as: M. Ansari, S. Mahdavikia, H. Eslami et al., Fabrication and characterization of magnesium-based nanocomposites reinforced with Baghdadite and carbon nanotubes for orthopaedical applications, Journal of Magnesium and Alloys, https://doi.org/10.1016/j.jma.2024.12.004